Contents lists available at ScienceDirect

Applied Catalysis B: Environmental

journal homepage: www.elsevier.com/locate/apcatb

Uniformed core-shell FeSe$_{2+x}$@C nanocube superlattices for Fenton-like reaction: Coordinative roles of cation and anion

Qiang Zhong [a],[1], Yue Sun [a],[1], Shixi Wu [b], Chenmin Xu [a], Shaogui Yang [a],[*], Yazi Liu [a], Dunyu Sun [a], Bing Yang [a], Yinhao Dai [a], Chengdu Qi [a], Zhe Xu [a], Huan He [a],[*], Shiyin Li [a], Shaobin Wang [c],[*]

[a] School of Environment, Nanjing Normal University, Nanjing, Jiangsu 210023, PR China
[b] School of Environmental Studies, China University of Geosciences, Wuhan 430074, PR China
[c] School of Chemical Engineering and Advanced Materials, The University of Adelaide, Adelaide, SA 5005, Australia

ARTICLE INFO

ABSTRACT

Simultaneously adjusting the coordination environment of Fenton-like catalysts and engineering their architectures is a viable strategy to promote catalytic reaction. Herein, two-dimensional (2D) porous core-shell FeSe$_{2+x}$@C nanocube superlattices (NCSLs) with unsaturated selenium are for the first time prepared via one-step selenization of Fe$_3$O$_4$@C NCSLs and tested for peroxymonosulfate (PMS)-based Fenton-like reaction. The 2D porous superlattice structure can preferably expand Fe sites exposure and accelerate the large-scale transport and utilization of nanocrystals. The unsaturated selenium can optimize the electronic state of cationic Fe, not only promoting the Fe^{3+}/Fe^{2+} cycle, regulating PMS adsorption, and improving the charge density, but also accelerating interfacial electron transport of the catalyst to lower the energy barrier of PMS decomposition to yield SO$_4^{\bullet-}$. This work demonstrates a new application of nanocrystal superlattices and provides more insights to active components of catalyst design for enhancing catalytic activity via structural control and coordination engineering in various application scenarios.

1. Introduction

With the rapid development of urbanization and industrialization, water pollution has seriously endangered human health and the ecosystem [1]. Sulfate radical (SO$_4^{\bullet-}$) based advanced oxidation processes (SR-AOPs) by activating peroxymonosulfate (PMS) have been considered to be one of the most powerful technologies for pollution remediation [2–4]. Among various activation methods, transition metal catalysis is appealing owing to a facile operation and low energy consumption [5]. Notably, homogeneous iron catalysts have great advantages in PMS activation because of their environmental friendliness and low economic cost, but suffer from iron sludge production and its separation [6]. In this regard, heterogeneous catalysis is recognized to be a promising alternative [7], and the development of a novel Fe-based heterogeneous catalyst with a high activity to overcome the kinetic and thermodynamic constraints is strongly desirable.

Iron-based selenides have displayed outstanding catalytic activities in electrochemical energy storage and conversion [8,9]. Recently, FeSe$_2$ nanoparticles were suggested to show performance in PMS activation, which revealed a potential application for iron-based selenides in environmental catalysis [10,11]. Notwithstanding little progress has been made. Moreover, FeSe$_2$ based catalysts still display limited catalytic activity, i.e., the deficient inherent electric conductivity, inadequate active sites from underdeveloped architecture, sluggish kinetics of the Fe^{3+}/Fe^{2+} redox cycle, and limited surface chemical activity in SR-AOPs. Consequently, it is highly imperative and challenging to construct FeSe$_2$-based catalysts with rapid electron transfer, abundant catalytic sites, rapid Fe^{3+}/Fe^{2+} cycle, and proper electronic state for high-efficiency PMS activation.

It is widely acknowledged that morphological architecture of a catalyst exhibits a significant impact on its catalytic performance [12–14]. Practically, the exposure of catalytic centers and mass transport during catalysis greatly rely on the structural characteristics of the catalyst [15–17]. Self-assembly of preformed nanocrystals (NCs) into two dimensional (2D) superlattices supplies a promising path for producing materials with tailored architectures and potentially

---

programmable characteristics [16,18,19]. Owing to the close-packed of NCs and their tunable coupling interactions, NC superlattices usually display collective/synergistic and increased physicochemical characteristics that are not available in an individual NC or disordered/agglomerated NC assemblies [20,21]. 2D superlattice structure also exhibits a high specific surface area, which easily exposes more catalytic sites without restriction on mass transport [22]. Besides, a thin porous carbon coating derived from the surface-capping ligands not only promotes charge transfer but also ensures the mechanical rigidity of the 2D superlattices [12]. Thus, 2D structured superlattices are a class of promising candidates for multifunctional applications. Notably, 2D superlattices have been partially investigated in sensors [23], optoelectronics [24,25], and energy storage [26,27]. Nevertheless, building superlattice materials from $FeSe_2$ based NCs keeps a great challenge, and such a superior structure has not been exploited in the field of environmental catalysis.

In catalysis, the coordination environment and electronic structure of metal ions in a transition metal compound are of significance, deciding the consequent intrinsic catalytic activity [28–30]. That is, regulating coordination environment of the reaction sites is an important means to improve the catalyst activity. However, most studies only focus on the function of metal cations, ignoring the anion. Notably, selenium species exhibits multiple valences in iron-based selenides [28, 31]. Low-valence selenium theoretically can serve as an electron donor to facilitate redox of active centers, indicating that the form of selenium in metal selenides has an important effect on the redox of the metal itself [10,11]. In addition, similar to unsaturated sulfur [32–34], unsaturated selenium easily builds an acidic microenvironment on the catalyst surface, which is beneficial to the stable Fe^{3+}/Fe^{2+} cycling and generation of sulfate radicals [29,32,35]. More importantly, the incorporated selenium probably adjusts the electronic structure of Fe catalytic sites and lowers charge delivery resistance from Fe to the contaminant. Therefore, it can be inferred that the form and content of anionic selenium species have a crucial influence on the catalytic activity of the catalyst. As far as we know, the relevant study on regulation of the catalytic activity of metal active centers by controlling the content and form of anions has seldom been reported so far, thus motivating a more detailed exploration.

In this study, we constructed 2D $FeSe_{2+x}$ @C nanocube superlattices (NCSLs) with different degrees of selenization via one-step selenization of carbon-coated Fe_3O_4 NCSLs, realizing PMS activation with high efficiency. The unique pore-structured 2D superlattices are favorable to improving mass diffusion and exposing more reaction sites. In addition, the introduced unsaturated selenium can not only build an acidic microenvironment on the catalyst surface, but also accelerate the redox of iron as well as adjust its electronic structure, thereby improving the catalyst activity. This work provides a scalable and versatile path for fabricating 2D $FeSe_{2+x}$ @C NCSLs catalysts and demonstrates their Fenton-like catalysis, which are of interest for a broad range of applications.

2. Experimental procedures

2.1. Chemicals and reagents

All the chemicals were of analytical grade and used without further purification unless otherwise specified. Ferricchloride hexahydrate ($FeCl_3 \cdot 6 H_2O$), diatrizioc acid (DIA), nafion (10 wt%), and 2,2,6,6-tetramethyl-4-piperidine (TEMP) were obtained from Sigma-Aldrich. Sodium oleate was purchased from TCI. Selenium powder, tert-butanol (TBA), ethanol (EtOH), methanol (MeOH), peroxymonosulfate (PMS, $2KHSO_5 \cdot KHSO_4 \cdot K_2SO_4$), 4-hydroxy-2,2,6,6-tetramethylpiperidine-N-oxyl (TEMPOL), and L-histidine were purchased from Sinopharm Chemical Reagent Co., Ltd, Shanghai, China. Deionized (DI) water with a resistivity of 18.2 MΩ●cm^{-1} was used in all of the experiments.

2.2. Synthesis of 2D Fe_3O_4@C NCSLs

In a typical procedure, 0.72 g $FeCl_3 \cdot 6 H_2O$, 2 mL deionized water, and 2.44 g of sodium oleate were mixed thoroughly. The resulting mixture was aged at 85 °C for 3 h, and then was mixed with 20 g of sodium sulfate powder. Subsequently, the reaction mixture was calcined at 600 °C under N_2 atmosphere for 3 h. After being cooled down naturally, the product of 2D Fe_3O_4 @C NCSLs was obtained by washing with deionized water three times and dried at 100 °C for 6 h. In addition, pure Fe_3O_4 was also prepared following the same procedure, except that sodium sulfate and sodium oleate were not used. In addition, to verify the superiority of 2D Fe_3O_4 @C NCSLs, we synthesized 3D Fe_3O_4 @C nanocomposites. The synthesis was the same as that of 2D Fe_3O_4 @C NCSLs described above except that sodium sulfate powder was not added.

2.3. Synthesis of 2D $FeSe_{2+x}$@C NCSLs

In a typical synthesis, the as-obtained 2D Fe_3O_4 @C NCSLs and Se powder with different ratios (1:2, 1:3, 1:4, 1:5) were put at the opposite corner of a quartz boat. Subsequently, the quartz boat was transferred into a tube furnace and selenization was executed at 360 °C for 8 h under the atmosphere of H_2/Ar (5 vol% of H_2) gas with a heat rate of 5 °C min^{-1}. Afterward, 2D $FeSe_{2+x}$ @C NCSLs were obtained. Besides, the composites synthesized with different mass ratios of 2D Fe_3O_4 @C: Se powder (1:2, 1:3, 1:4, 1:5) were named as $FeSe_{2+x}$ @C-2, $FeSe_{2+x}$ @C-3, $FeSe_{2+x}$ @C-4, and $FeSe_{2+x}$ @C-5, respectively. As a comparison, pure $FeSe_2$, 3D $FeSe_{2+x}$ @C-3, and $FeSe_{2+x}$ @C-3 M nanocomposites were also obtained via the same selenization process (Fe_3O_4 or 3D Fe_3O_4 @C or Fe-MOFS: Se powder =1:3) using pure Fe_3O_4, 3D Fe_3O_4 @C, and Fe-MOFs nanocomposites as the precursors, respectively. In addition, in order to control the content of selenium more precisely and investigate the effect of selenium content on catalytic activity, we heated the as-prepared $FeSe_{2+x}$ @C-3 NCSLs at 300 °C for 1 h to obtain a sample with a certain selenium content (marked as $FeSe_{2+x}$ @C-3A).

2.4. Synthesis of 2D FeSe@C, Fe_3Se_4@C, and Fe_7Se_8@C NCSLs

For 2D FeSe@C NCSLs, the as-obtained 2D Fe_3O_4 @C NCSLs and Se powder with a ratio (1:6) were put at the opposite corners of a quartz boat. Subsequently, the quartz boat was transferred into a tube furnace and selenization was executed at 600 °C for 3 h under the atmosphere of Ar gas with a heat rate of 2 °C min^{-1}. Afterward, 2D FeSe@C NCSLs was obtained.

For 2D Fe_3Se_4 @C NCSLs, the as-obtained 2D Fe_3O_4 @C NCSLs and Se powder with a ratio (1:2) were put at the opposite corners of a quartz boat. Subsequently, the quartz boat was transferred into a tube furnace and selenization was executed at 350 °C for 1 h and subsequent 450 °C for 2 h under the atmosphere of H_2/Ar (5 vol% of H_2) gas with a heat rate of 5 °C min^{-1}. Afterward, 2D Fe_3Se_4 @C NCSLs was obtained.

For 2D Fe_7Se_8 @C NCSLs, the as-obtained 2D Fe_3O_4 @C NCSLs and Se powder with a ratio (1:7.5) were put at the opposite corners of a quartz boat. Subsequently, the quartz boat was transferred into a tube furnace and selenization was executed at 450 °C for 4 h and subsequent 600 °C for 2 h under the atmosphere of Ar gas with a heat rate of 2 °C min^{-1}. Afterward, 2D Fe_7Se_8 @C NCSLs was obtained.

2.5. Material characterizations

Powder X-ray diffraction (XRD) measurements were conducted to investigate the crystal structure of the synthesized catalysts. The surface morphologies were observed by field emission scanning electron microscopy (FESEM, Hitachi SU8200) and transmission electron microscopy (TEM, Hitachi H7700). Moreover, the material microstructures were investigated by high-resolution TEM (HRTEM, Talos F200X) operated at 200 kV. Atomic force microscopy (AFM) images were

obtained from a Bruker Atomic Force Microscope under trapping-mode. Surface potential distribution of the as-prepared samples were measured by the Kelvin probe force microscopy (KPFM) at a scanning probe microscope (SPM) system. The composition and element valence states of the catalyst were determined by X-ray photoelectron spectroscopy (XPS) using a Perkin Elmer PHI-5000 C ESCA system. Raman spectra were recorded with an XploRA Raman system. Thermogravimetric analysis (TGA) was executed with a heating rate of $10\,^\circ C\,min^{-1}$ under an air flux. Fourier transform infrared (FT-IR) spectroscopy were conducted on a Bruker Vertex 70 using KBr pellets. The specific surface area and pore volume were determined by a Micromeritics ASAP-2020 instrument. H_2 temperature-programmed reduction (H_2-TPR) and NH_3 temperature-programmed desorption (NH_3-TPD) were performed using a micromeritics AutoChem II 2920 analyzer. The content of Fe and Se in the as-synthesized catalysts were tested by an inductively coupled plasma atomic emission spectrometer (ICP-AES). The free radicals were recorded on an electron paramagnetic resonance (EPR) spectrometer (Bruker E500, Germany).

2.6. Electrochemical measurement

All the electrochemical properties were conducted in a standard three-electrode electrochemical cell comprising a catalyst-modified fluorine-tin oxide (FTO) glass as the working electrode, a platinum wire as the counter electrode, and Ag/AgCl as the reference electrode. In addition, during the test, a mixture of 0.5 M Na_2SO_4 or 3 M KOH and 1.5 mM PMS was used as the electrolyte. The working electrode was prepared using 10 mg catalyst and 40 μL of nafion solution (10 wt%) dispersed in 1 mL deionized water. Thereafter, the mixture was pipetted onto a $1 \times 1\,cm^2$ of FTO and the electrode was dried in ambient air before use. All potentials reported in our work were referenced to a reversible hydrogen electrode (RHE). Electrochemical impedance spectra (EIS), linear sweep voltammetry (LSV), Tafel curve, cyclic voltammetry (CV), Mott−Schottky (MS) plots, chronoamperometries were carried out by using an electrochemical station (SP-150, Bio-Logic SAS, France).

2.7. Calculations of FeSe₂ and carbon contents of 2D FeSe₂₊ₓ@C NCSLs from TGA curves

TGA was conducted in air, and the weight loss of 2D $FeSe_{2+x}$ @C nanocube superlattices from 400° to 800 °C corresponds to the oxidation of $FeSe_2$ to Fe_2O_3 and SeO_2 and the combustion of carbon. The detail calculation procedure was provided in Text S1. Therefore, the weight percentage of $FeSe_2$ and carbon can be calculated accordingly.

2.8. Theoretical calculations details

The density functional theory (DFT) computations were carried out by a Vienna ab initio simulation package (VASP) using the projector augmented wave (PAW) method [36]. The exchange correlation potential was represented by the Perdew–Burke–Ernzerhof (PBE) functional within the generalized gradient approximation (GGA) [37]. The cutoff energy is set to 500 eV, and k-point sampling grid is set to $2 \times 3 \times 1$. The structures were relaxed until the convergence tolerances of energy and force were less than 1.0×10^{-5} eV/atom and 2.0×10^{-2} eV/Å, respectively. The vacuum layer is set to 15 Å. The DFT-D3 method is used to describe the van der Waals interaction [38]. Moreover, we employed Hubbard U potential to describe the Coulomb electron interaction precisely, with the U value of Fe set to 5 eV [39,40]. The adsorption energy (E_{ab}) of HSO_5^- on catalyst surface can be calculated by Eq. (1):

$$E_{ab} = E(\text{sub} + HSO_5^-) - E(\text{sub}) - E(HSO_5^-) \tag{1}$$

Where, E (sub + HSO_5^-) is the total energy of the HSO_5^- after adsorption

on catalyst surface, E (sub) is the total energy of the catalyst, E (HSO_5^-) is the total energy of the HSO_5^-.

2.9. Catalytic activity measurements

The catalytic degradation tests were executed in 50 mL flat-bottom beaker at room temperature of $22 \pm 1\,^\circ$C. Specifically, 10 mg of as-prepared catalysts was evenly dispersed in 50 mL DIA (20 mg/L) solution and stirring in dark for 20 min to establish the adsorption-desorption equilibrium. Following, a predetermined amount of PMS was added to initiate the catalytic degradation reaction, and the pH of the reaction solution was not adjusted artificially which fluctuated within the range of 2.8–2.9 in most cases due to the presence of PMS. At predetermined time intervals, 0.8 mL reaction solution was withdrawn, filtered by 0.22 μm nylon filter membrane and quenched with 0.2 mL methanol to terminate the catalytic reaction. The residual DIA was detected by a high-performance liquid chromatography with a C18 column at λ_{DAD}= 254 nm. The mobile phase was a mixture of 0.1% formic acid water solution/methanol (90/10, vol/vol). In addition, the degradation intermediates of DIA are identified by HPLC/MS. The gradient program of mobile phase is shown in Fig. S1 at a flow rate of 0.5 mL·min^{-1}. The total organic carbon (TOC) was detected by an Analytic Jena multi-N/C 3100 TOC. In order to comprehend the reaction kinetics, the kinetic rate constants (k_{obs}) of DIA degradation were further analyzed. The equation as followed:

$$\ln (C_0/C_t) = k_{obs} \cdot t \tag{2}$$

where, t is the reaction time, C_0 and C_t represent the concentrations of DIA at original and different reaction time, respectively, and k_{obs} is the first-order kinetic constant (min^{-1}). Moreover, it is worth noting that the pH value of the reaction system was not further adjusted unless otherwise stated. To avoid any misleading conclusions, buffers were not used. In the recycling test, the catalyst was collected after each run, fully washed with ethanol and water and dried before the next recycling.

3. Results and discussions

3.1. Physicochemical properties of catalysts

The synthesis procedures of 2D $FeSe_{2+x}$ @C NCSLs are schematically illustrated in Fig. 1(a). Typically, 2D layered carbon-coated Fe_3O_4 @C NCSLs were synthesized based on a salt-templated method [22], via the megathermal pyrolysis (under N_2 atmosphere) of iron oleate complexes on the surface of thermally stable Na_2SO_4 particles (Fig. S2(a-b)), where the Na_2SO_4 particles act as the template to prevent complex agglomeration during annealing and iron oleate complexes were used as the precursor of both ferrite and carbon. Afterward, the as-prepared 2D layered carbon-coated Fe_3O_4 @C NCSLs were thermally induced with Se powder at 360 °C under H_2/Ar (5 vol% of H_2) atmosphere (Fig. S3), and the possible reaction can be expressed as (1) $H_2 + Se \rightarrow H_2Se$; (2) $2Fe_3O_4 + 16\,H_2Se \rightarrow 6FeSe_2\,(s) + 16\,H_2\,(g) + 4SeO_2\,(g)$, and the 2D $FeSe_{2+x}$ @C NCSLs was obtained after that. Notably, the selenization of 2D Fe_3O_4 @C NCSLs initiates the conversion of 2D solid Fe_3O_4 @C NCSLs to 2D porous $FeSe_{2+x}$ @C NCSLs via the Kirkendall diffusion effect while reserving the cube shape and positioning.

Atomic force microscopy (AFM) measurements (Fig. 1(b)) indicated that 2D Fe_3O_4 @C NCSLs have a layered nanosheet structure with a thickness approximately 148 nm based on its height profile. Field emission scanning electron microscopy (FESEM) and transmission electron microscopy (TEM) suggest that 2D Fe_3O_4 @C NCSLs show the single layer tightly packed nanocubic lattice with brilliant structural ordering (Fig. 1(c-d)). Strikingly, the Fe_3O_4 @C nanocubes are considerably similar in magnitude, with an average edge length of 28.8 nm (Fig. S4(a)). Energy-dispersive X-ray spectroscopy (EDS) mapping and elemental analysis (Fig. S4(b-c)) suggest the uniform distributions of Fe,
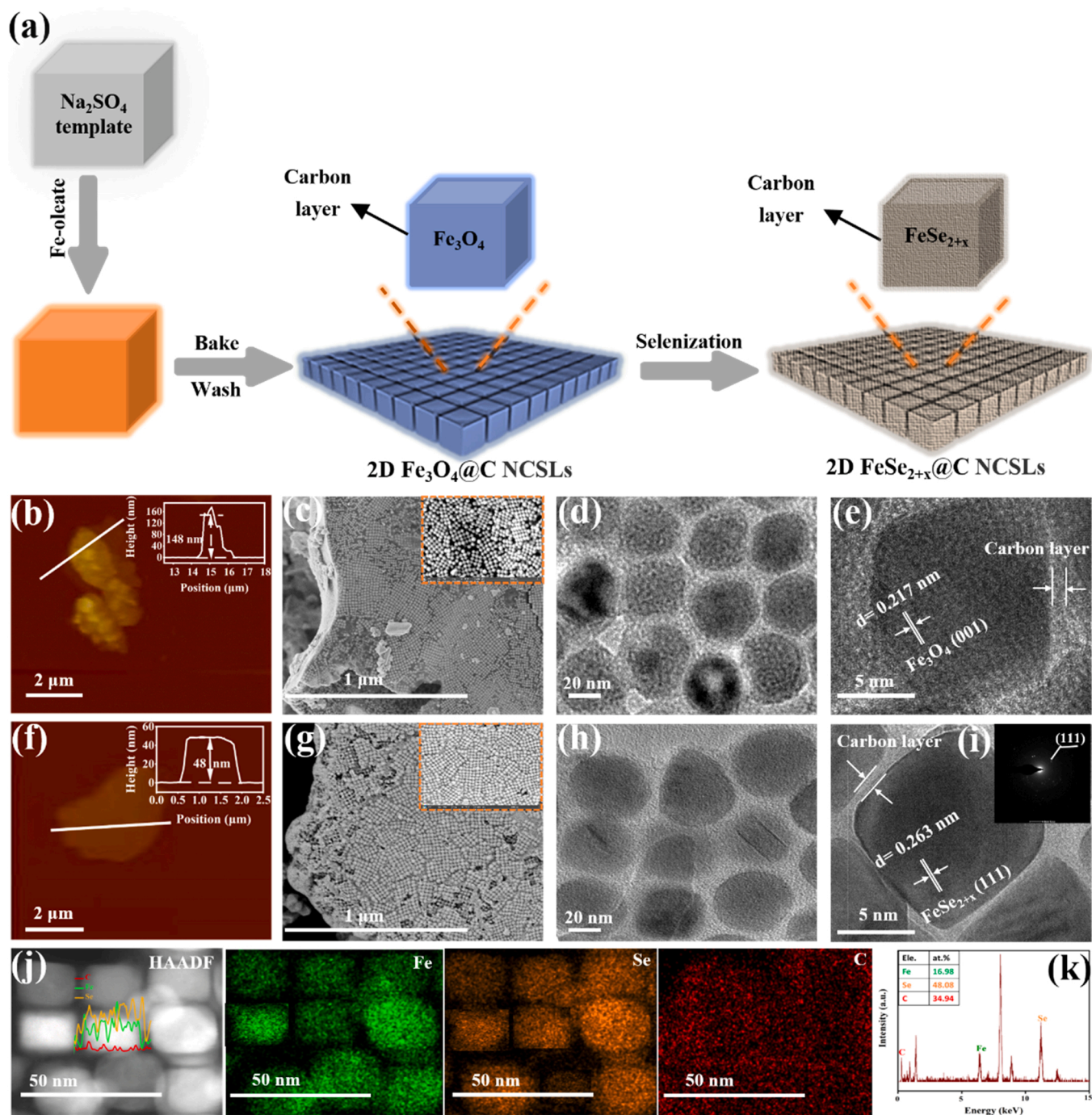
Fig. 1. (a) Schematic of the preparation of 2D $FeSe_{2+x}$ @C-3 NCSLs. (b) AFM (inset is the height profile of 2D Fe_3O_4 @C NCSLs along the arrow line in (b)), (c) FESEM and its magnification(inset), (d) TEM, and (e) HRTEM images of 2D Fe_3O_4 @C NCSLs. (f) AFM (inset is the height profile of 2D $FeSe_{2+x}$ @C-3 NCSLs along the arrow line in (f)), (g) FESEM and its magnification(inset), (h) TEM, (i) HRTEM (Inset for the FFT image), and (j) HAADF-STEM image and corresponding line scan and element mapping of 2D $FeSe_{2+x}$ @C-3 NCSLs, (k) EDS images of 2D $FeSe_{2+x}$ @C-3 NCSLs.

O, and C throughout 2D Fe_3O_4 @C NCSLs with a Fe/O molar ratio of approximately 3:4. High-resolution TEM (HRTEM) further verifies the existence of Fe_3O_4 (001) facet, with a facet distance of 0.217 nm (Fig. 1 (e)). Moreover, it is also observed that Fe_3O_4 nanocubes are isolated by a thin carbon shell, derived from thermolysis of the surfactant layer. To observe the carbon layer structure in detail, we removed the embedded Fe_3O_4 nanocubes via acid etching, resulting in hollow 2D carbon sheets consisted of few-layer graphitic carbon (Fig. S5(a-d)). Thus, it can be concluded that Fe_3O_4 nanocrystals uniformly confined in a highly ordered carbon network are favorably synthesized.

Subsequently, 2D porous $FeSe_{2+x}$ @C-3 NCSLs were obtained by in-situ selenization using Se powder (Fig. S3). In addition, 3D agglomerated $FeSe_{2+x}$ @C-3 nanocomposites, pure $FeSe_2$, and $FeSe_{2+x}$ @C-3 M derived from Fe-MOFs were also prepared, and their morphology can be observed (Fig. S6(a-f)). AFM (Fig. 1(f)) shows that the thickness of 2D $FeSe_{2+x}$ @C NCSLs (48 nm) is significantly reduced compared to 2D Fe_3O_4 @C NCSLs. Moreover, the in-situ selenization process did not disrupt the 2D structure of the surface superlattices, instead making the surface rougher due to H_2Se gas generation (Fig. 1(g)). Inspiringly, these geometry and structural advantages not only facilitate mass diffusion

and catalytic site exposure, but also promote electron transfer, thereby endowing 2D FeSe$_{2+x}$ @C-3 NCSLs potential advantages as a catalyst for contaminant removal [41–43].

Notably, the conversion of 2D Fe$_3$O$_4$ @C NCSLs to 2D FeSe$_{2+x}$ @C-3 NCSLs resulted in an increased superlattice size. The average edge length of FeSe$_{2+x}$ @C nanocubes is 30.1 nm (Fig. S7(a)), larger than Fe$_3$O$_4$ @C nanocubes. Interestingly, despite of the increased nanocube size, the pattern and ordered arrangement retained the morphology of the pristine Fe$_3$O$_4$ @C nanocubes during selenization (Fig. 1(h)). Moreover, the outer carbon shell still maintains the tight lattice order

even after acid washing (Fig. S7(b-c)), indicating its mechanical rigidity. Such structural features can prevent the dissolution of metal ions and enhance the stability of the catalyst [44,45]. HRTEM and fast Fourier transform (FFT) pattern (Fig. 1(i)) confirm that the FeSe$_2$ nanocubes were highly crystalline, and the D-spacing of 0.263 nm is referred to the (111) facet. The elemental mapping and line scan results (Fig. 1(j)) verify the uniform distributions of Fe, Se, and C across the 2D FeSe$_{2+x}$ @C-3 NCSLs. Moreover, the EDS spectrum (Fig. 1(k)) of 2D FeSe$_{2+x}$ @C-3 NCSLs indicates the ratio of Se/Fe at ~2.83, powerfully revealing the Se-enriched property of the considerable exposure of unsaturated Se
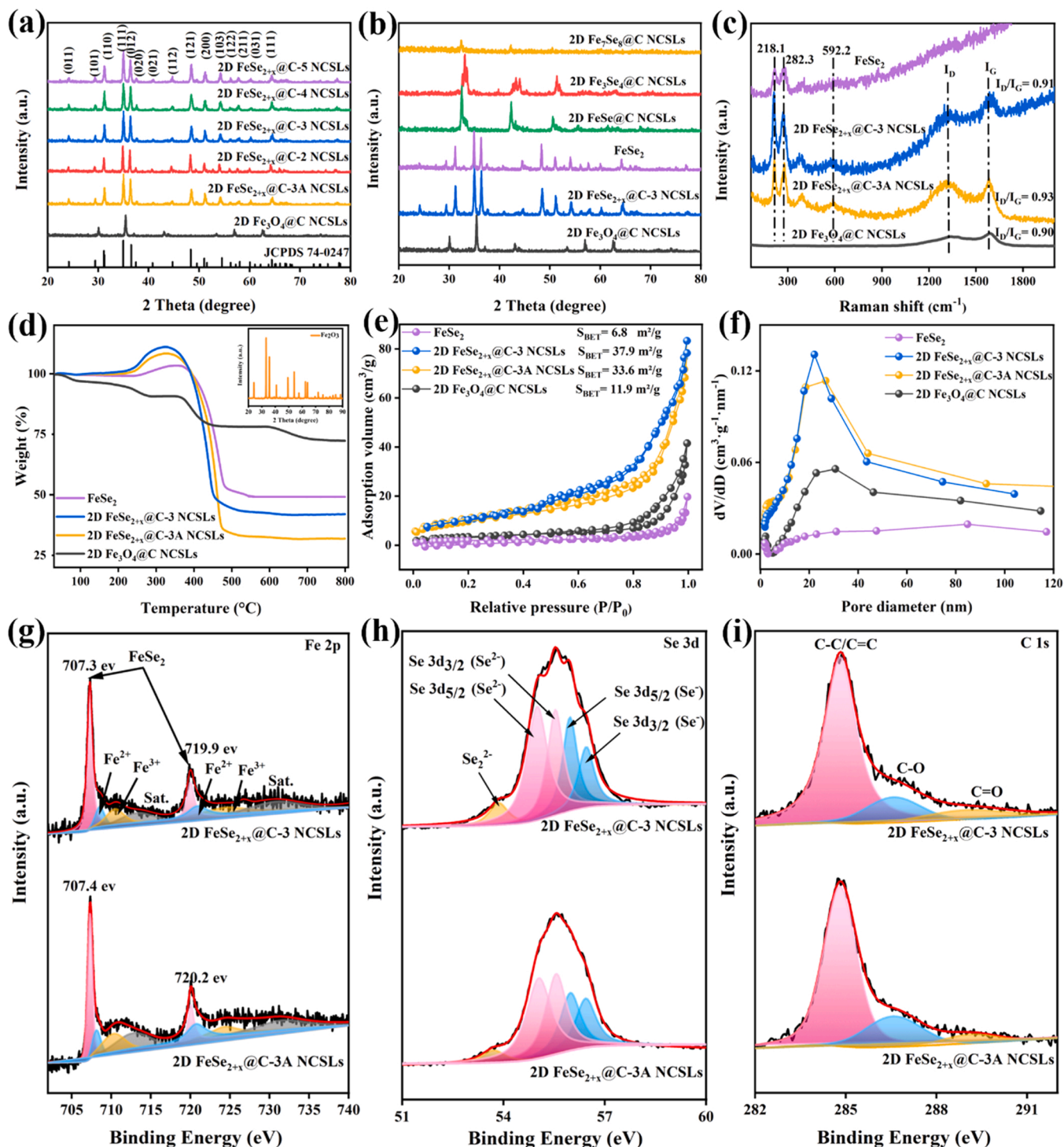

Fig. 2. (a) and (b) XRD patterns, (c) Raman spectra, (d) TGA curves (inset is the XRD patterns of Fe$_2$O$_3$), (e) N$_2$ adsorption/desorption isotherms, and (f) pore size distributions of as-prepared catalysts. High-resolution XPS spectra of 2D FeSe$_{2+x}$ @C-3 and FeSe$_{2+x}$ @C-3A NCSLs: (g) Fe 2p, (h) Se 3d, and (i) C 1 s.

sites [29]. Similar results can be obtained from FESEM elemental mapping and EDS (Fig. S8 (a-b)).

In addition, in order to control the content of selenium more effectively, we annealed the as-synthesized 2D $FeSe_{2+x}$ @C-3 NCSLs at 300 °C (the melting point of Se and below the temperature of the reaction) under argon atmosphere for 1 h (denoted as 2D $FeSe_{2+x}$ @C-3A NCSLs). After the processing, the geometry, structure, and elemental dispersion of the 2D $FeSe_{2+x}$ @C-3A NCSLs remained unchanged (Fig. S9 (a-e)). As expected, EDS data (Fig. S9 (f)) indicates the Se/Fe ratio close to 2.23 is lower than that of 2D $FeSe_{2+x}$ @C-3 NCSLs. To get the actual Se/Fe atomic ratio, we executed ICP-AES measurements (Table S1). Obviously, compared with 2D $FeSe_{2+x}$ @C-3A NCSLs (Se/Fe: 2.46), 2D $FeSe_{2+x}$ @C-3 NCSLs own the higher Se/Fe ratio of 3.10 owing to its Se-enriched property. Notably, the current fabrication procedure of 2D $FeSe_{2+x}$ @C-3 NCSLs without any solvents is facile to scale up (Fig. S10) for their subsequent applications.

The conversion of 2D Fe_3O_4 @C NCSLs into 2D $FeSe_{2+x}$ @C NCSLs was clearly identified by XRD patterns. By controlling the content of selenium powder, 2D $FeSe_{2+x}$ @C NCSLs with different degrees of selenization were prepared, and the as-synthesized catalysts exhibit the diffraction peaks indexed well to orthorhombic ferroselite (JCPDS No: 74–0247) [46] (Fig. 2(a)). Notably, the diffraction peaks of Fe_3O_4 disappear completely in all the as-prepared samples, indicating a complete conversion to 2D $FeSe_{2+x}$ @C NCSLs. Furthermore, the 2D $FeSe_{2+x}$ @C-3A NCSLs obtained by further annealing still retain the characteristic diffraction peaks of 2D $FeSe_{2+x}$ @C-3 NCSLs, indicating no change of crystal structure and consistence with the SEM and TEM results. Moreover, as a comparison, other Fe-based selenides derived from 2D Fe_3O_4 @C NCSLs selenization and pure $FeSe_2$ were also successfully prepared, and their XRD patterns are assigned to pure $FeSe_2$, 2D FeSe@C NCSLs [47], 2D Fe_3Se_4 @C NCSLs [48], 2D Fe_7Se_8 @C NCSLs [49], respectively (Fig. 2(b)).

Raman spectra of the as-obtained catalysts are depicted in Fig. 2(c). For $FeSe_2$, 2D $FeSe_{2+x}$ @C-3 NCSLs, and 2D $FeSe_{2+x}$ @C-3A NCSLs, the peaks at 218.1, 282.3, and 592.2 cm^{-1} were corresponded to the characteristic vibration modes of $FeSe_2$ [31], which are in good agreement with the XRD results. Besides, 2D $FeSe_{2+x}$ @C-3 NCSLs, 2D $FeSe_{2+x}$ @C-3A NCSLs, and 2D Fe_3O_4 @C NCSLs display D (~1347 cm^{-1}) and G bands (~1580 cm^{-1}) with an analogous I_D/I_G value [42], demonstrating that the selenization of 2D Fe_3O_4 @C NCSLs and subsequent heat treatment had a negligible effect on the carbon network structure (Fig. 2(c)). In addition, thermogravimetric analysis (TGA) was applied to calculate the content of each component of the as-prepared catalysts. Fig. 2(d) displays the weight loss of the samples at the temperature up to 800 °C, corresponding to the conversion of $FeSe_2$ or Fe_3O_4 to Fe_2O_3 and the combustion of carbon [50]. The final product (Fe_2O_3) is obviously depicted in the inset of Fig. 2(d). Therefore, the accurate content of $FeSe_2$ in 2D $FeSe_{2+x}$ @C-3 NCSLs was calculated to be 73.13%, higher than $FeSe_{2+x}$ @C-3A NCSLs (68.43%), implying that the higher content of unsaturated selenium in 2D $FeSe_{2+x}$ @C-3 NCSLs (Detailed calculation process is demonstrated in Supporting Information).

N_2 adsorption-desorption isotherms of 2D $FeSe_{2+x}$ @C-3 NCSLs display a specific surface area of 37.9 m^2 g^{-1} with large mesopores centering around 22 nm, similar to 2D $FeSe_{2+x}$ @C-3A NCSLs (Fig. 2(e-f)). However, the specific surface area and pore distribution are much higher than those of 2D Fe_3O_4 @C NCSLs and $FeSe_2$. Such a structural feature can provide sufficient contact sites for the reaction medium and reduce mass transfer resistance [51]. Therefore, it is beneficial to improving the catalytic activity of 2D porous $FeSe_{2+x}$ @C-3 NCSLs.

The elemental composition and chemical states of 2D $FeSe_{2+x}$ @C-3 NCSLs and 2D $FeSe_{2+x}$ @C-3A NCSLs were explored using X-ray photoelectron spectroscopy (XPS). The coexistence of Fe, Se, and C elements can be observed by the survey spectra (Fig. S11), showing consistence with the EDS analysis. The relevant high-resolution XPS spectra are depicted in Fig. 2(g-i). Fe 2p spectra (Fig. 2(g)) of 2D $FeSe_{2+x}$ @C-3 NCSLs display two predominant peaks at 707.3 and 719.9 eV,

corresponding to Fe $2p_{3/2}$ and Fe $2p_{1/2}$ of $FeSe_2$, respectively [31,50]. Whereas the other characteristic peaks belong to iron oxides formed by surface oxidation of $FeSe_2$, indicating the presence of trace Fe^{2+} and Fe^{3+} oxidation states in $FeSe_2$. Notably, the iron oxides could not be observed in the XRD pattern, indicating that rather weak oxidation occurred on the 2D $FeSe_{2+x}$ @C-3 NCSLs surface. Similar trends can be observed on 2D $FeSe_{2+x}$ @C-3A NCSLs. Fe 2p peaks of 2D $FeSe_{2+x}$ @C-3 disclose a left shift for lower binding energy compared of 2D $FeSe_{2+x}$ @C-3A NCSLs, indicating increased charge density at Fe sites and the electric interaction between Fe and Se. Moreover, the microstructure features of unsaturated Se-enriched 2D $FeSe_{2+x}$ @C-3 and 2D $FeSe_{2+x}$ @C-3A NCSLs can be profoundly exposed by Se 3d spectra (Fig. 2(h)). There were two forms of selenium i.e., selenide (Se_2^{2-}/Se^{2-}, 53.8, 54.9 and 55.5 eV), and monoselenide (Se^{1-}, 55.9 and 56.1 eV) [28,29]. Moreover, 2D $FeSe_{2+x}$ @C-3A NCSLs present a lower proportion of Se atoms (Se^{1-}, Se_2^{2-}/Se^{2-}), revealing a decreased Se amount on the surface after annealing treatment. Notably, the coordinatively unsaturated selenide, i.e., Se_2^{2-}/Se^{2-}, dominates the Se species in 2D $FeSe_{2+x}$ @C-3 NCSLs.

Therefore, XPS with EDS, ICP-AES, and TGA results unequivocally verify that a certain amount of unsaturated Se atoms have been effectively incorporated into the 2D $FeSe_{2+x}$ @C-3 NCSLs surface. Hence, it can be speculated that 2D $FeSe_{2+x}$ @C-3 NCSLs can display a remarkably superior catalytic performance. Besides, C 1 s spectra (Fig. 2(i)) can be deconvoluted into three peaks at 284.8, 286.5, and 288.9 eV, assigned to the C-C/C=C, C-O, and C=O, respectively [19,52]. In summary, all the above characterizations demonstrate the successful preparation of 2D porous $FeSe_{2+x}$ @C NCSLs with enriched unsaturated selenium.

3.2. Catalytic performance in Fenton-like reactions

The catalytic activity of the as-prepared materials was evaluated by removing diatrizoic acid (DIA) via PMS activation. DIA is a typical emerging contaminant with endocrine-disrupting effects [53]. Fig. 3 (a-b) indicated that both adsorption and PMS itself could hardly decrease DIA amount, proving that the DIA removal is mainly due to the catalytic degradation process. In addition, as depicted in Fig. 3(a) and Fig. S12, 2D $FeSe_{2+x}$ @C-3 NCSLs exhibited the highest removal rate of DIA with a rate constant (k_{obs}) of 0.207 min^{-1}, which is 26, 13.9, 15.3, and 16.2 times higher than 2D Fe_3O_4 @C, FeSe@C, Fe_3Se_4 @C, and Fe_7Se_8 @C NCSLs, respectively. Further, the total organic carbon (TOC) analysis proved that parts of DIA were mineralized to CO_2 and H_2O in the 2D $FeSe_{2+x}$ @C-3 NCSLs/PMS system (Fig. S13).

Moreover, Fig. S14 revealed that superlattice carbon (obtained by pickling 2D $FeSe_{2+x}$ @C-3 NCSLs) and pure $FeSe_2$ exhibit a limited removal rate of DIA. Notably, 2D $FeSe_{2+x}$ @C NCSLs with different degrees of selenization (i.e., 2D $FeSe_{2+x}$ @C-2, 2D $FeSe_{2+x}$ @C-3, 2D $FeSe_{2+x}$ @C-4, and $FeSe_{2+x}$ @C-5 NCSLs, Fig. S15) exhibited volcano-like plots of the removal rates of DIA, with the maximum k_{obs} (0.207 min^{-1}) and removal rate (100%) from 2D $FeSe_{2+x}$ @C-3 NCSLs. Thus, the content of selenium in iron-based selenides has a crucial effect on their catalytic activity (Fig. 3 (b)). Moreover, the removal rate of 2D $FeSe_{2+x}$ @C-3A NCSLs is significantly lower than that of 2D $FeSe_{2+x}$ @C-3 NCSLs, suggesting that unsaturated selenium may affect the electronic structure and coordination environment of the Fe active centers as well as catalytic activity. Intriguingly, compared with 3D $FeSe_{2+x}$ @C-3 composites, 2D $FeSe_{2+x}$ @C-3 NCSLs exhibit a better DIA removal rate (Fig. 3(b)), which reflects the advantages of 2D porous superlattice with exposing more active sites and improving mass diffusion.

In addition, compared with randomly dispersed cubic lattices (FeSe$_{2+x}$ @C-3 M), 2D $FeSe_{2+x}$ @C-3 NCSLs composed of ordered cubic lattices can be regarded as larger nanoreactors, showing better removal efficiency of DIA (Fig. 3(b)). The above results further illustrate the structural advantages of 2D porous $FeSe_{2+x}$ @C-3 NCSLs in PMS activation for pollutant removal. Consequently, it was reasonable to speculate that both unsaturated selenium content and structural regulation
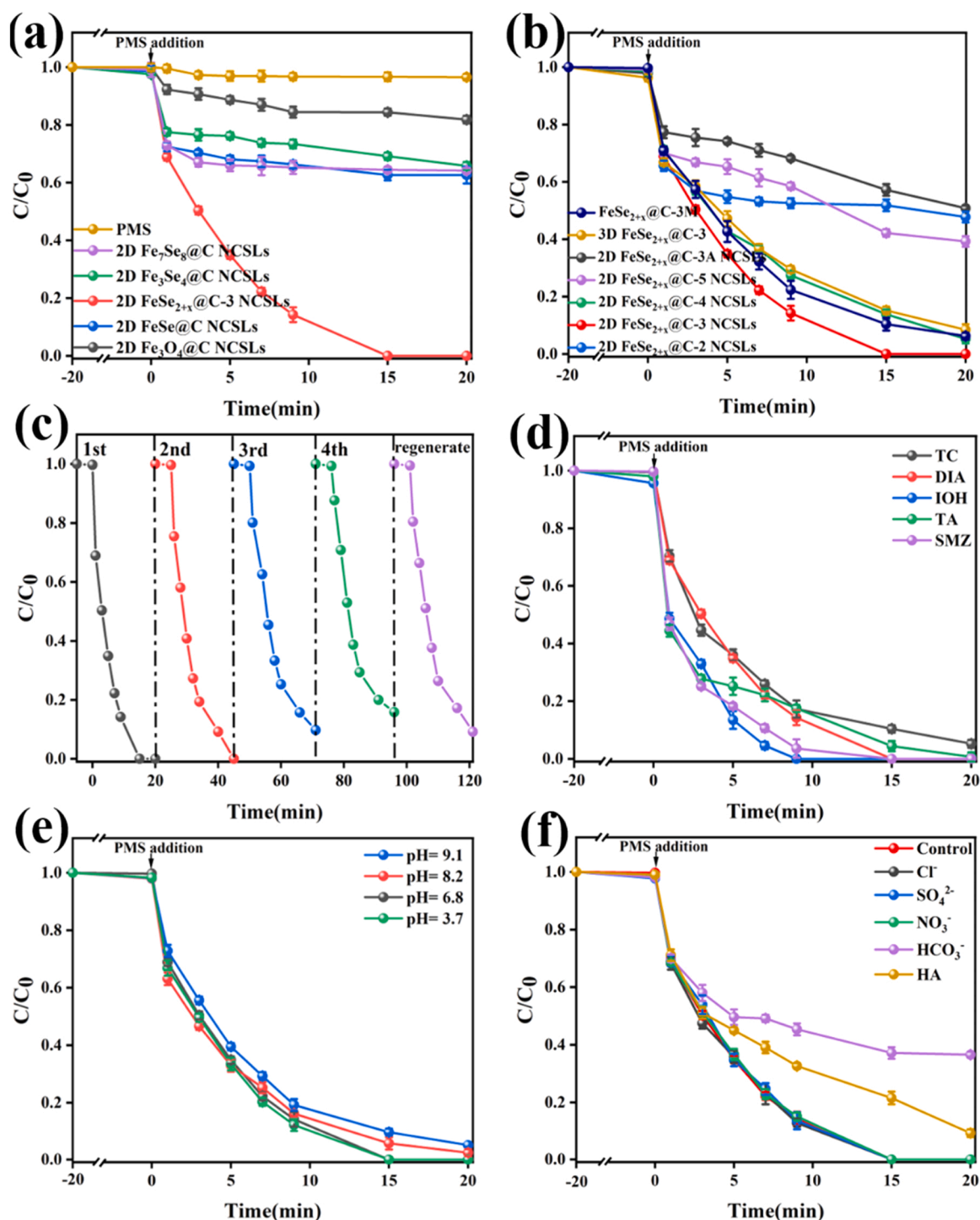
Fig. 3. (a) and (b) Degradation curves of DIA under different catalyst conditions, (c) cycling tests of 2D FeSe$_{2+x}$ @C-3 NCSLs for DIA degradation, (d) degradation of diverse pollutants in the 2D FeSe$_{2+x}$ @C-3 NCSLs/PMS system, (e) degradation of DIA at different initial pH values in 2D FeSe$_{2+x}$ @C-3 NCSLs/PMS system, (f) effect of inorganic ions on DIA degradation in 2D FeSe$_{2+x}$ @C-3 NCSLs/PMS system. Experimental conditions: [DIA]$_0$ = 20.0 mg/L, [PMS]$_0$ = 1.5 mM, [catalyst]$_0$ = 0.2 g/L, [inorganic ions]$_0$ = 5 mM, [HA]$_0$ = 5 mg/L.

play crucial roles in the catalytic activity, in which unsaturated selenium was the leading factor.

Besides, 2D FeSe$_{2+x}$ @C-3 NCSLs/PMS system exhibits excellent reusability for DIA degradation (Fig. 3(c)). The removal rate slightly decreases from 100.0% to 84.1% after four successive runs, which is mainly ascribed to the degradation intermediates of DIA covering the surface of the catalyst. Interestingly, after washing with ethanol and subjected to the fifth cycle, its removal rate of DIA was recovered to

~90% due to re-exposure of more active sites. Fe and Se leaching during the reuse experiments ranged in 0.044–0.763 and 0.004–0.009 mg/L, respectively (Fig. S16), far below the standard for drinking water (i.e., 10 mg/L for Fe and 0.01 mg/L for Se). This may be attributed to the porous carbon in the outer layer of 2D FeSe$_{2+x}$ @C-3 NCSLs, which not only improves the cyclic stability of the catalyst, but also reduces ion dissolution [54]. Furthermore, the dissolved Fe^{2+} (0.763 mg/L) exhibits a limited contribution in DIA removal, demonstrating that

heterogeneous catalysis dominates the degradation process (Fig. S17).

The XRD, Raman, XPS, SEM, and TEM analyses show no evident difference in the microstructure and crystallinity of 2D $FeSe_{2+x}$ @C-3 NCSLs before and after the reaction (Fig. S18(a-e)), demonstrating the decent structural stability. Additionally, Fig. 3(d) displays that the 2D $FeSe_{2+x}$ @C-3 NCSLs/PMS system can decompose a wide array of refractory organic pollutants, including tetracycline (TC), iohexol (IOH), terramycin (TM), and sulfamethazine (SMZ). Consequently, the novel system reveals a widespread capability for remediation of multiple organic contaminants in water. Moreover, the system displays a wide pH adaptability, and the removal efficiency still remains high even under alkaline conditions (Fig. 3(e)). It can be attributed to many unsaturated Se sites (one/two-coordination) on the catalyst surface, as the unsaturated Se can trap H^+ from solution to form an acidic microenvironment on the catalyst surface [29,32,35]. Therefore, an acidic microenvironment is beneficial to improve the catalytic activity of the catalyst via automatically adjusting the environment to an acidic pH.

Furthermore, the 2D $FeSe_{2+x}$ @C-3 NCSLs/PMS system exhibits an excellent anti-interference ability. Although excess humic acid (HA) and HCO_3^- show slight inhibition, the presence of environmental-relevant anions (i.e., Cl^-, SO_4^{2-}, NO_3^-) present a negligible effect on DIA degradation (Fig. 3(f)). More importantly, 2D $FeSe_{2+x}$ @C-3 NCSLs exhibit a slight weak activity for DIA degradation in natural waters (Tap water, the Yangtze River, and the Xuanwu Lake) compared with deionized water (Fig. S20(d)), demonstrating its potential in practical applications. Besides, 2D $FeSe_{2+x}$ @C-3 NCSLs exhibit the exceptionally high catalytic activity, which is compelling in the comparison with other metal-based catalysts used in heterogeneous PMS-assisted Fenton-like reactions (TableS2). Thus, 2D $FeSe_{2+x}$ @C-3 NCSLs/PMS system has the potential to eliminate organic contaminant in aqueous solution with high efficiency. Density functional theory (DFT) calculations combined with liquid chromatography–mass spectrometry (LC-MS) was also employed to determine the degradation intermediates and possible degradation pathways of DIA in 2D $FeSe_{2+x}$ @C-3 NCSLs/PMS system (Fig. S20–S22)

as shown further below.

3.3. Identification of reactive species

To further verify the radical products in 2D $FeSe_{2+x}$ @C-3 NCSLs/PMS system during DIA degradation, we implemented the scavenging tests. The DIA degradation was significantly depressed by methanol (MeOH, a quencher for $\cdot OH$ and $SO_4^{\bullet -}$) [55], while it was only weakly inhibited by tert-butyl alcohol (TBA, a $\cdot OH$ quencher) [10], L-histidine (a $^1O_2$ quencher), and 4-hydroxy-2,2,6,6-tetramethylpiperidine-N-oxyl (TEMPOL, a $O_2^{\bullet -}$ quencher) [10,56], demonstrating $SO_4^{\bullet -}$ as a dominant species in DIA degradation (Fig. 4(a)). Consistent results were received by electron paramagnetic resonance (EPR) characterizations. The EPR signals of DMPO-$\cdot OH$ and DMPO-$SO_4^{\bullet -}$ adducts became stronger when 2D $FeSe_{2+x}$ @C-3 NCSLs and PMS co-presented and faded upon DIA addition (Fig. 4(b)). In addition, the signal intensity of DMPO$-SO_4^{\bullet -}$ is significantly stronger than that of DMPO-$\cdot OH$. However, the slight change of TEMP-$^1O_2$ and DMPO-$O_2^{\bullet -}$ in the PMS system after catalyst and/or DIA addition indicate a minor role of $^1O_2$ and $O_2^{\bullet -}$ in the DIA degradation (Fig. S23(a-b)). Therefore, it is confirmed that $SO_4^{\bullet -}$ is primarily responsible for the DIA degradation, and $\cdot OH$, $^1O_2$, and $O_2^{\bullet -}$ play a minor role.

Notably, the time-resolved TEMP-$^1O_2$ and DMPO-$O_2^{\bullet -}$ signals appear much stronger in the 2D $FeSe_{2+x}$ @C-3A NCSLs/PMS system than those in 2D $FeSe_{2+x}$ @C-3 NCSLs/PMS system (Fig. 4(d-e)). However, the DMPO-$SO_4^{\bullet -}$ and DMPO-$\cdot OH$ signals in the 2D $FeSe_{2+x}$ @C-3 NCSLs/PMS system are obviously stronger (Fig. 4(c)). We noted $SO_4^{\bullet -}$ and $\cdot OH$ generation in the 2D $FeSe_{2+x}$ @C-3A NCSLs/PMS system was rapid at the primary stage, but quickly saturated. Differently, $SO_4^{\bullet -}$ and $\cdot OH$ in the 2D $FeSe_{2+x}$ @C-3 NCSLs/PMS system could gradually increase without saturation. It may be due to the fact that an appropriate amount of unsaturated selenium can promote the rapid cycling of Fe^{3+}/Fe^{2+}, thereby accelerating the free radical production. In addition, the acidic microenvironment on the 2D $FeSe_{2+x}$ @C-3 NCSLs surface also
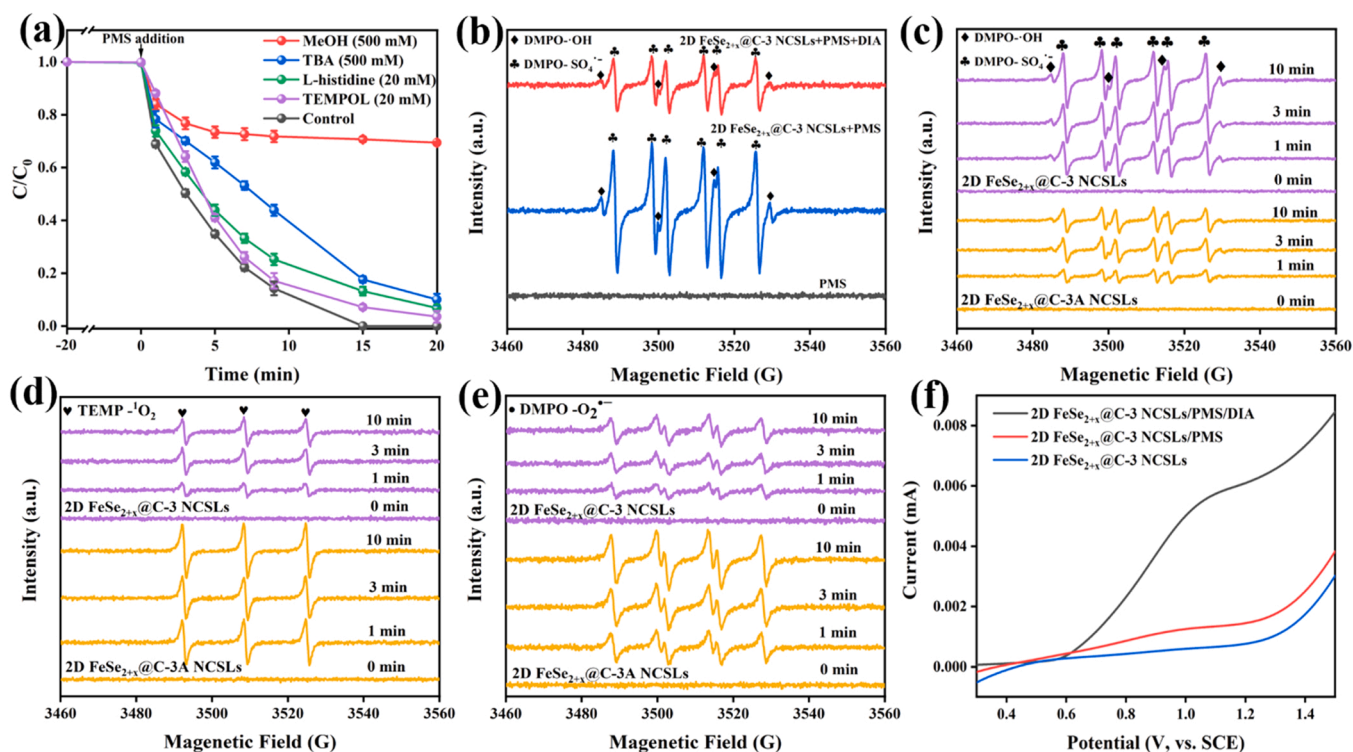

Fig. 4. (a) Effects of radical scavengers under different quenching conditions in 2D $FeSe_{2+x}$ @C-3 NCSLs/PMS system. Experimental conditions: $[DIA]_0 = 20.0$ mg/L, $[PMS]_0 = 1.5$ mM, $[catalyst]_0 = 0.2$ g/L. (b), (c), (d), and (e) EPR spectra of activated PMS systems of different reaction systems, (f) linear sweep voltammetry (LSV) curves of different reaction systems.

contributes to the stable existence of $SO_4^{•-}$. Thus, the appropriate amount of unsaturated selenium rivets on 2D $FeSe_{2+x}$ @C-3 NCSLs surface can improve the catalytic activity and adjust the pathway of chemical reactions.

Furthermore, a mediated electron transfer is a possible oxidative degradation mechanism [57]. The linear sweep voltammetry (LSV) (Fig. 4(f)) further indicated that the current of the DIA oxidation peak was greatly increased upon PMS addition, indicating PMS-promoted electron transfer from DIA to 2D $FeSe_{2+x}$ @C-3 NCSLs. Similar results can also be obtained from in-situ Raman (Fig. S24). Notably, the electron transfer-mediated pollutant degradation process accounts for a small proportion, which can be seen from the free radical quenching experiments.

3.4. Predominant active metal species for PMS activation

To verify that Fe serves as the main reactive site producing active species, we performed the poisoning experiment using potassium thiocyanate (KSCN) as a complexing agent [58]. The removal rate of DIA was significantly reduced when KSCN was added (Fig. 5(a)). As KSCN is easily deposited on Fe sites (Fig. S25(a)), the above effect indicates that Fe was the dominant active site in activating PMS. Moreover, 2, 2′-bipyridine (BPY), a chelating agent of Fe^{2+} (Fig. S25(b)), to prevent Fe^{2+} from reacting with PMS, was employed to monitor the direct activation of PMS via Fe^{2+} in 2D $FeSe_{2+x}$ @C-3 NCSLs/PMS system [11] (Fig. 5(b)). As expected, the degradation efficiency of DIA reduced from 100% to 18.6% in the existence of BPY (3 mM). Notably, BPY and KSCN by themselves do not activate PMS to degrade DIA. Besides, the area of
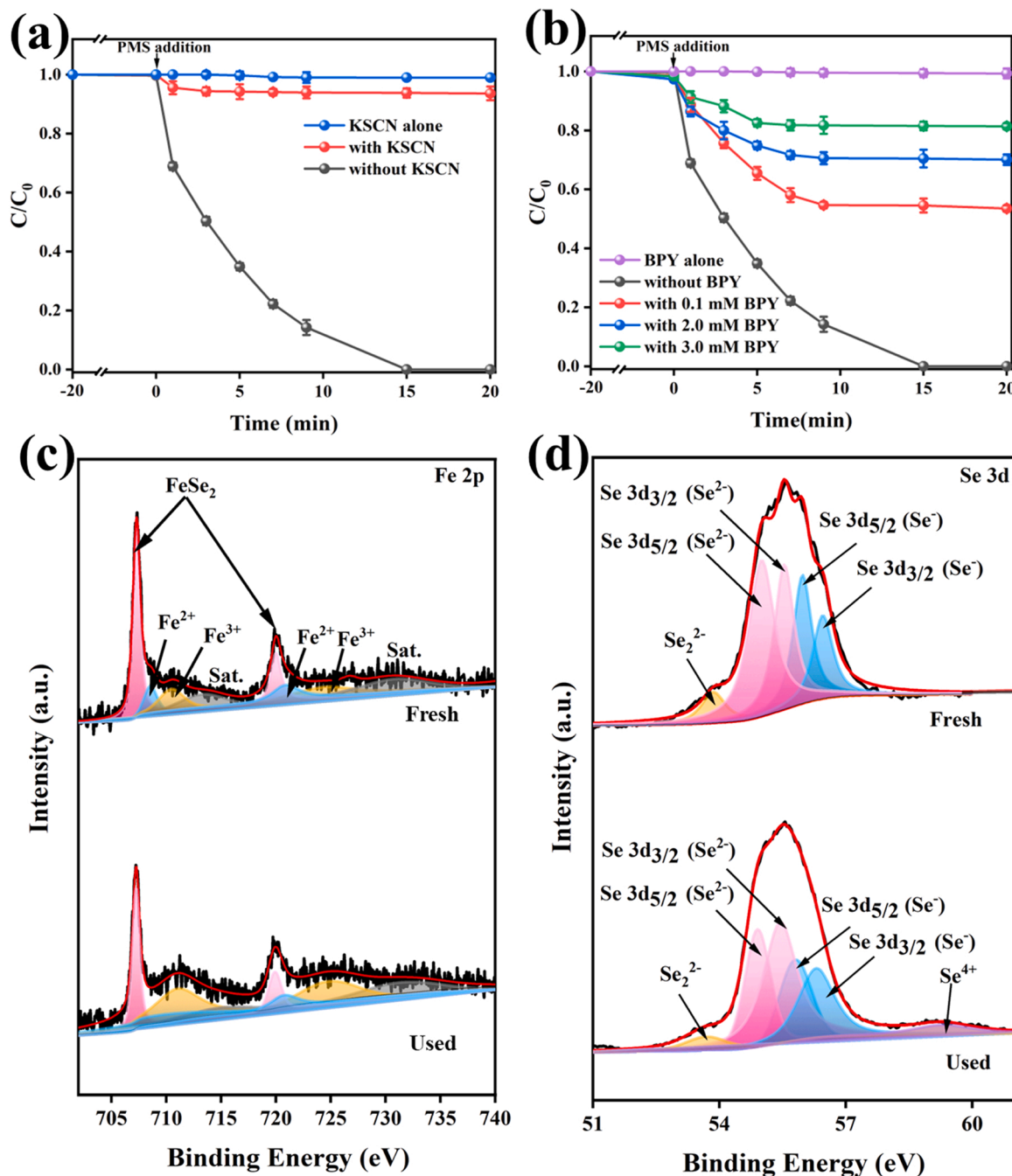

Fig. 5. (a) Fe toxicity tests and (b) effects of 2,2′-bipyridine (BPY) as a surface Fe^{2+} chelator on DIA removal in $FeSe_{2+x}$ @C-3/PMS system. Experimental conditions: $[DIA]_0 = 20.0$ mg/L, $[PMS]_0 = 1.5$ mM, $[catalyst]_0 = 0.2$ g/L. High-resolution XPS spectra of (c) Fe 2p and (d) Se 3d for fresh and used $FeSe_{2+x}$ @C-3.

the Fe^{3+} peak in XPS Fe 2p spectra (Fig. 5(c)) increased slightly after reaction, indicating that the oxidation of Fe species occurs during PMS activation. The above results indicated that Fe^{2+} on the surface of 2D $FeSe_{2+x}$ @C-3 NCSLs acts as the main electron donor in PMS activation. Consequently, it is worth noting that the regeneration of Fe^{2+} is the rate-limiting step in 2D $FeSe_{2+x}$ @C-3 NCSLs/PMS system.

Furthermore, XPS Se 3d spectra displayed that the area of low valence selenium decreased while some high-valence selenium appeared during PMS activation (Fig. 5(d)), revealing that selenium may act as an electron donor to participate in the activation of PMS or the regeneration of Fe^{2+}. To confirm that Se species can promote the regeneration of Fe^{2+}, different concentrations of Fe^{3+} were added to the 2D $FeSe_{2+x}$ @C-3 NCSLs/PMS/DIA system (Fig. 6(a)). As expected, the removal rate of DIA gradually increased with the enhanced Fe^{3+} concentration, while the removal of DIA by Fe^{3+}/PMS system was rather limited. Similar observations can be obtained from a ZnSe/PMS/Fe^{3+} system (Fig. S26). All the findings indicated that Fe^{3+} can be captured and reduced to Fe^{2+} by low valence Se species, improving the catalytic activity.

In addition, phenanthroline colorimetry was used to detect the generation of Fe^{2+} in the $FeSe_{2+x}$ @C-3/Fe^{3+} reaction solution. A remarkable Fe^{2+} signal at 510 nm in 2D $FeSe_{2+x}$ @C-3 NCSLs/Fe^{3+} system exhibited (Fig. 6(b)), revealing that Fe^{2+} was actually generated in reaction solution. Besides, the Fe^{2+} generation on the 2D $FeSe_{2+x}$ @C-3 NCSLs catalyst surface was further verified by filtering the reaction suspension before adding the phenanthroline. Interestingly, no distinct Fe^{2+} signal peak was observed in the filtered solution, indicating that

free Fe^{3+} was captured and reduced to Fe^{2+} on the surface of 2D $FeSe_{2+x}$ @C-3 NCSLs. Compared with 2D $FeSe_{2+x}$ @C-3 NCSLs/PMS system, with the increase of Fe^{3+} in 2D $FeSe_{2+x}$ @C-3A NCSLs/PMS system, DIA removal rate was not significantly improved, which indicates that the content of selenium has a crucial effect on the catalytic activity (Fig. S27). Besides, ZnSe was prepared via a similar method to the 2D $FeSe_{2+x}$ @C-3 NCSLs. Since the cationic Zn cannot effectively activate PMS, it was used to verify the electron transfer between the Se species and PMS. About 22% of DIA can be degraded in ZnSe/PMS system (Fig. S26), implying that selenium can provide partial electrons to activate PMS.

In-situ Raman analysis was employed to disclose the affinity between the catalyst and PMS. As described in Fig. 6(c), the peaks at 876 and 1055 cm^{-1}, 975 cm^{-1} belong to HSO_5^- of PMS and S=O bonds of SO_4^{2-}, respectively [59]. Consequently, the change of peak intensity can be used to evaluate the decomposition rate of PMS to a certain extent, and the lower peak intensity reflects the higher decomposition rate of PMS. It can be noticed that, with the existence of 2D $FeSe_{2+x}$ @C-3 NCSLs, the PMS peak intensity becomes the smallest, reflecting the fastest PMS consumption by the catalyst. This trend is in good agreement with the degradation kinetics of DIA. Furthermore, in the presence of the catalyst, the PMS characteristic peaks show a red-shift to varying degrees compared to the PMS solution alone. This suggests that electron transfer may have occurred between Fe and PMS. Among them, 2D $FeSe_{2+x}$ @C-3 NCSLs have the largest red-shift, which may be due to the fact that more Fe^{2+} species are produced in 2D $FeSe_{2+x}$ @C-3 NCSLs, and that the
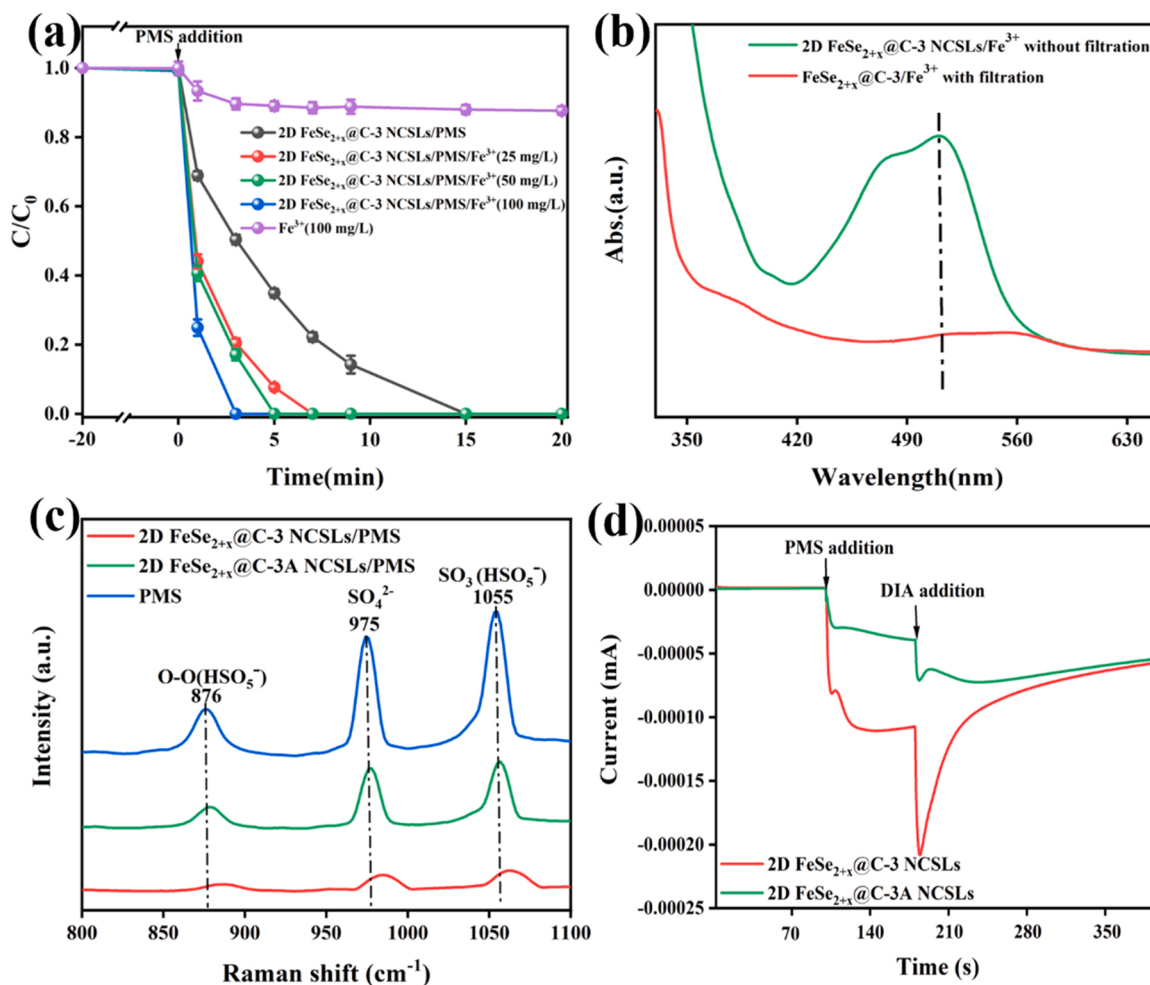

Fig. 6. (a) effects of Fe^{3+} ion addition on DIA removal in $FeSe_{2+x}$ @C-3/PMS. Experimental conditions: $[DIA]_0 = 20.0$ mg/L, $[PMS]_0 = 1.5$ mM, $[catalyst]_0 = 0.2$ g/L. (b) UV–vis spectra of $FeSe_{2+x}$ @C-3/Fe^{3+} suspension and filtrate in the presence of phenanthroline. (c) In-situ Raman spectra and (d) i-t curves of different reaction systems.

interface reaction between Fe^{2+} and PMS is stronger. To further support this, an i-t curve was performed and showed the similar results (Fig. 6 (d)).

3.5. The nature of high activity of 2D FeSe$_{2+x}$@C-3 NCSLs

All the above results unveiled that unsaturated selenium played critical roles in the enhancement of catalytic activity. To better understand the role of unsaturated selenium, we executed electrochemical tests to characterize its electronic properties. As depicted in Mott-Schottky analysis (Fig. S28), the flat band potential (E_{FB}) of the catalyst can be gained through an intercept, and the corresponding E_{FB} values of 2D FeSe$_{2+x}$@C-3 NCSLs and 2D FeSe$_{2+x}$@C-3A NCSLs are - 1.123 and - 0.837 V, respectively. Notably, E_{FB} reflects the position of Fermi level, the barrier height for charge transfer, and the viability to be an electron donor in reaction solution [10]. As illustrated of Fig. 7(a), a lower E_{FB} value indicates a higher position of Fermi level, revealing that 2D FeSe$_{2+x}$@C-3 NCSLs are more likely to supply charges to initiate the chain reaction of PMS activation, modulate interfacial energetics, and lower the electron transfer barrier.

Moreover, the cyclic voltammetry (CV) curves (Fig. 7(b)) were measured to reveal the redox properties of the catalyst [60]. Two weak peaks (an oxidation peak (E^{ox}) and a reduction peak (E^{red}) at 0.33 V) emerged in the CV curve of 2D FeSe$_{2+x}$@C-3A NCSLs, reflecting inferior Fe^{3+}/Fe^{2+} redox reactions in 2D FeSe$_{2+x}$@C-3A NCSLs. Conversely, the quasi-reversible CV curve of 2D FeSe$_{2+x}$@C-3 NCSLs exhibits the higher current intensity at E^{ox} and E^{red}, especially for E^{red}, indicating that the Fe^{3+}/Fe^{2+} redox cycle on FeSe$_{2+x}$@C-3 is easily triggered and facilitated with more unsaturated Se. Furthermore, the half-wave potential ($E_{1/2}$) (i.e., [E^{red} + E^{ox}]/2) of FeSe$_{2+x}$@C-3 is about 0.25 V, lower than that of 2D FeSe$_{2+x}$@C-3A NCSLs (0.26 V) and implying the boosted reduction of Fe^{3+} in the FeSe$_{2+x}$@C-3 system [61].

Additionally, the electron transfer in heterogeneous Fenton-like reactions was tested by electrochemical impedance spectroscopy (EIS) (Fig. 7(c)). Obviously, compared to the 2D FeSe$_{2+x}$@C-3A NCSLs, the Nyquist plot diameter of 2D FeSe$_{2+x}$@C-3 NCSLs is smaller, verifying its faster electron transport capability and better catalytic activity [10]. Similarly, Tafel diagrams (Fig. 7(d)) displayed that the corrosion potentials of 2D FeSe$_{2+x}$@C-3 NCSLs and 2D FeSe$_{2+x}$@C-3A NCSLs are − 0.75 and − 0.68 V, respectively, indicating that the former exhibits lower charge transfer resistance [62]. Furthermore, the EIS and Tafel results (Fig. S29(a-b)) of 2D Fe$_3$O$_4$@C NCSLs and 2D FeSe$_{2+x}$@C-3 NCSLs indicate that anionic selenium can accelerate electron transfer. This phenomenon can be attributed to the metal-like properties of selenium that can promote electron transfer [63].

The redox properties of the catalysts were further characterized using H$_2$-temperature programmed reduction (TPR) (Fig. 8(a)). Two typical peaks at 397.5 and 613.6 °C in the H$_2$-TPR curve of 2D FeSe$_{2+x}$@C-3 NCSLs, corresponding to the reduction of Fe^{3+} to Fe^{2+} and Fe^{2+} to Fe, respectively, display higher peak intensities and a slight shift towards lower temperatures compared to 2D FeSe$_{2+x}$@C-3A NCSLs [64]. Thus, more unsaturated selenium can enhance the reducibility of 2D FeSe$_{2+x}$@C-3 NCSLs, and improve the catalytic activity of the catalyst. Fourier transform infrared (FT-IR) spectroscopy shows that the surface hydroxyl stretching vibration peak of 2D FeSe$_{2+x}$@C-3 NCSLs at 3200–3400 cm^{-1} is significantly stronger than that of 2D FeSe$_{2+x}$@C-3A NCSLs (Fig. S30), indicating that 2D FeSe$_{2+x}$@C-3 NCSLs has stronger surface acidity [32] and that unsaturated selenium can
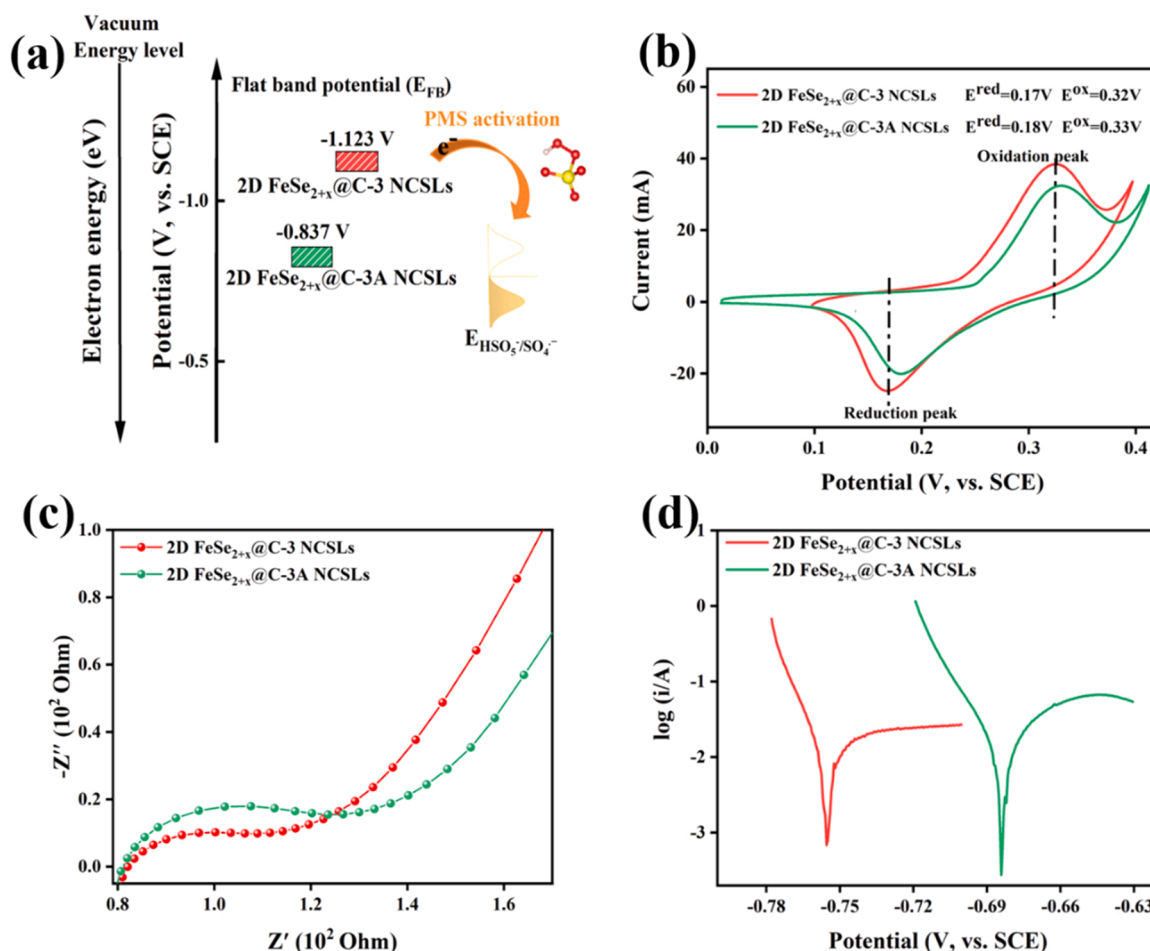

Fig. 7. (a) Flat band potential, (b) cyclic voltammetry (CV) curves, (c) EIS measurements and (d) Tafel diagrams of FeSe$_{2+x}$@C-3 and FeSe$_{2+x}$@C-3A.
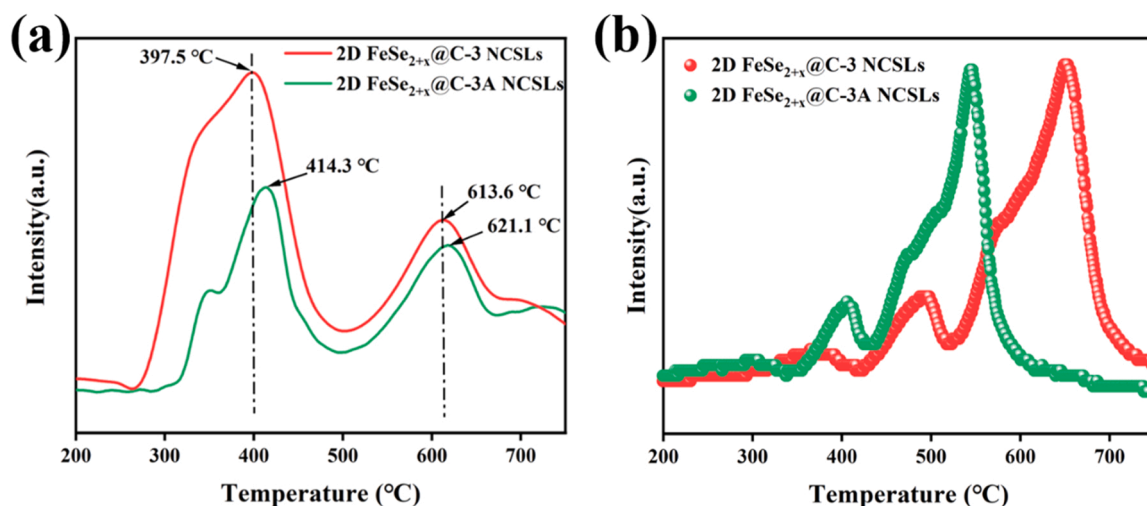
Fig. 8. (a) H_2-TPR, and (b) NH_3-TPD profiles of 2D $FeSe_{2+x}$ @C-3 and 2D $FeSe_{2+x}$ @C-3A NCSLs.

generate an acidic microenvironment on the catalyst surface.

In addition, NH_3-temperature programmed desorption (TPD) curve was used to verify the increase in the surface acidity of 2D $FeSe_{2+x}$ @C-3 NCSLs (Fig. 8(b)). 2D $FeSe_{2+x}$ @C-3 NCSLs and 2D $FeSe_{2+x}$ @C-3A NCSLs exhibited several peaks from about 350–750 °C. Compared with 2D $FeSe_{2+x}$ @C-3A NCSLs, 2D $FeSe_{2+x}$ @C-3 NCSLs have a larger shift of the peak to high temperature, indicating stronger surface acidity [65]. Therefore, the increased acidity of the catalyst surface is beneficial to 2D $FeSe_{2+x}$ @C-3 NCSLs surface for the stable Fe^{3+}/Fe^{2+} cycling in Fenton-like reactions. More importantly, the surface acidic microenvironment is conducive to the stable existence of sulfate radicals, which also explains the dominant active species to be sulfate radicals in the 2D $FeSe_{2+x}$ @C-3 NCSLs/PMS system.

DFT calculations were then engaged to further clarify the importance of unsaturated Se on tuning the electronic structure of Fe catalytic sites for PMS activation. Two different surface models, 2D $FeSe_2$ @C-3(111) NCSLs without unsaturated Se and 2D $FeSe_{2+x}$ @C-3(111) NCSLs with unsaturated Se, were constructed (Fig. S31(a-b)) as FFT and XRD analyses show the dominant (111) plane of $FeSe_2$ (Figs. 1(i) and 2(a)).

The charge density difference is firstly calculated in order to investigate the electronic structure of 2D $FeSe_{2+x}$ @C-3 NCSLs. As shown in Fig. 9(a-b), an overt charge accumulation around Fe species and charge depletion around Se components in 2D $FeSe_{2+x}$ @C-3 NCSLs system are clearly observed as compared with those in 2D $FeSe_2$ @C-3 NCSLs system. This demonstrates a strong interaction between Se and Fe for an electron transfer in 2D $FeSe_{2+x}$ @C-3 NCSLs. This calculation result is consistent with the XPS of Fe 2p. Furthermore, the Bader charge analysis displays an electron transfer of 0.13e from the surrounding Se atoms to Fe species in 2D $FeSe_{2+x}$ @C-3 NCSLs, while only 0.06e for 2D $FeSe_2$ @C-3 NCSLs, indicating that Fe species in the 2D $FeSe_{2+x}$ @C-3 NCSLs are more conducive to obtaining electrons and accelerating to initiate the subsequent reduction reactions. Moreover, the electronic properties of the catalyst were further analyzed using the density of states (DOS). Remarkably, 2D $FeSe_{2+x}$ @C-3 NCSLs display a more negative charge than 2D $FeSe_2$ @C-3 NCSLs, indicating that unsaturated selenium can increase the energy level of the catalyst and facilitate electrons to overcome the interfacial barrier. This trend is in accordance with their energetic feature (Fig. 7(a)). Moreover, the calculations of partial density of states (PDOS) indicated that the degree of charge overlaps of the Fe 3d and Se 4p orbitals in 2D $FeSe_{2+x}$ @C-3 NCSLs is larger than that in 2D $FeSe_2$ @C-3 NCSLs (Fig. 9(c-d)), which illustrates the stronger interaction and the easier electron transfer in 2D $FeSe_{2+x}$ @C-3 NCSLs. Besides, the D-band center of Fe of 2D $FeSe_{2+x}$ @C-3 NCSLs is closer to the Fermi level compared with 2D $FeSe_2$ @C-3A NCSLs, revealing that the introduction of unsaturated Se on the 2D $FeSe_{2+x}$ @C-3 NCSLs

results in a stronger PMS adsorption and high electron mobility (Fig. 9(c-d)). Besides, Fe in 2D $FeSe_{2+x}$ @C-3 NCSLs with improved 3d charge transition probability can easily supply charges during the catalytic reaction, and the 2D $FeSe_{2+x}$ @C-3 NCSLs exhibit a higher catalytic activation performance.

In addition, the charge density analysis further displays that the highly unoccupied e_g states of Fe in 2D $FeSe_{2+x}$ @C-3 NCSLs initiate electron delocalization at the Fe site at a much higher degree than that in 2D $FeSe_2$ @C-3 NCSLs (Fig. S32(a-d)). Similarly, the surface charge density was analyzed by the Kelvin probe force microscopy (KPFM), as depicted in (Fig. 9(e-f)) and (Fig. S33(a-b)). The surface potential of 2D $FeSe_{2+x}$ @C-3 NCSLs ($\Delta E = 410$ mV) is much higher than that of 2D $FeSe_2$ @C-3 NCSLs ($\Delta E = 140$ mV), further indicating that 2D $FeSe_{2+x}$ @C-3 NCSLs can provide more electrons to promote the PMS activation. Besides, the bond of PMS on two model surfaces is depicted in Fig. 9(g-h). The PMS adsorption energies (ΔE_{ads}) were calculated to be -3.40 and -3.06 eV, demonstrating that PMS adsorption is energetically favorable. Noticeably, the smaller ΔE_{ads} value of 2D $FeSe_{2+x}$ @C-3 NCSLs indicates a stronger chemical force on the surface (Fig. 9(g-h)). Furthermore, the peroxide bond(l_{o-o}) of PMS is lengthened from 1.47 to 1.48 Å after binding to 2D $FeSe_{2+x}$ @C-3 NCSLs (Fig. 9(g-h)), revealing that the catalyst with rich unsaturated Se is more conducive to the activation and cleavage of PMS.

Besides, Mulliken charge analysis was employed to explore the electron delivery between the active center and PMS (Fig. 9(g-h)). The charge density difference of PMS adsorption on catalysts further disclose that the unsaturated selenium site devotes to curtail the molecular distance for improved adsorption. The electron depletion area is mainly accumulated around Fe cations, providing the channel to accept electrons. Interestingly, it can be also observed that the electron loss of unsaturated Se atoms further illustrates the strong interaction between Se, Fe, and PMS (Fig. 9(h)). Similar results can be observed from LSV, in situ Raman spectroscopy, and PDOS of PMS adsorbed on the Fe centers (Fig. S34). Excitingly, the charge amount diverted from Fe sites to PMS was 0.93e on 2D $FeSe_{2+x}$ @C-3 NCSLs, which is much higher than that on 2D $FeSe_2$ @C-3 NCSLs (0.79e) (Fig. 9(g-h)). The differences in charge density resulted in a much easier cleavage of PMS to yield active species on 2D $FeSe_{2+x}$ @C-3 NCSLs.

Based on the above discussions of the systems and literature, the superior catalytic activity and stability of 2D $FeSe_{2+x}$ @C-3 NCSLs are ascribed to their inimitable structural characteristics (i.e., 2D layered geometry, closely ordered superlattice structure, and interconnected carbon network) and the presence of suitable amounts of unsaturated selenium (Fig. 10 and Fig. S35). The structural advantages can be reflected in the following points: (i) 2D layered geometry of $FeSe_{2+x}$ @C-3
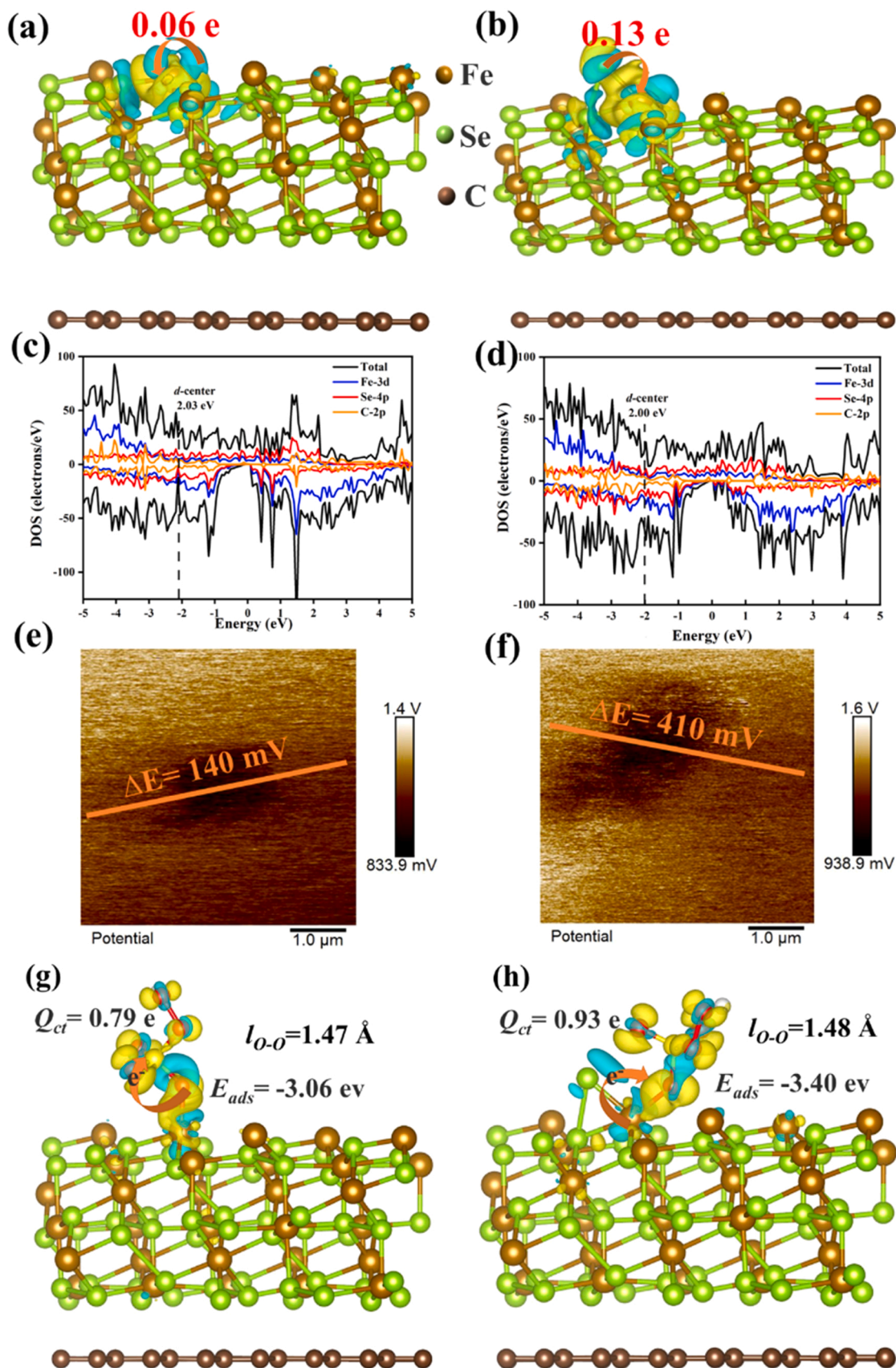
Fig. 9. (a) and (b) Different charge densities of 2D FeSe$_2$ @C-3(111) NCSLs and 2D FeSe$_{2+x}$ @C-3(111) NCSLs, the density of states of (c) 2D FeSe$_2$ @C-3(111) NCSLs and (d) 2D FeSe$_{2+x}$ @C-3(111) NCSLs surfaces, surface potential of (e) 2D FeSe$_2$ @C-3(111) NCSLs and (f) 2D FeSe$_{2+x}$ @C-3(111) NCSLs detected with KPFM, Charge density difference of PMS adsorption model on (g) 2D FeSe$_2$ @C-3(111) NCSLs and (h) 2D FeSe$_{2+x}$ @C-3(111) NCSLs surfaces. (The red, yellow and white spheres represent O, S and H atoms, respectively, the yellow area and the sky-blue area represent the accumulation and loss of electrons, respectively).
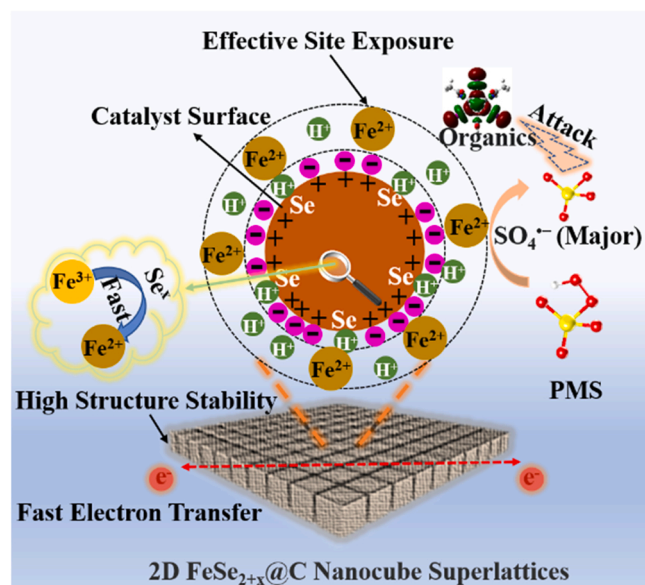
Fig. 10. The mechanism diagram of the Fenton-like reaction on 2D $FeSe_{2+x}$ @C-3 nanocube superlattices surface.

NCSLs promotes mass transfer and catalytic site exposure; (ii) the closely ordered superlattice structure can improve its stability during the reaction; (iii) the interconnected carbon network not only accelerates charge delivery but also impedes the agglomeration and ion dissolution of $FeSe_{2+x}$ @C nanocubes.

Overall, the positive influences of unsaturated selenium in superlattices are ascribed to the reasons as follows: (i) optimizing the adsorption of reaction medium on 2D $FeSe_{2+x}$ @C-3 NCSLs and improving PMS adsorption for stretching; (ii) lowering reaction energy barrier, thereby increasing the static energy of charge transfer; (iii) promoting the Fe^{3+}/Fe^{2+} cycling; (iv) modulating interfacial physicochemical properties of 2D $FeSe_{2+x}$ @C-3 NCSLs (i.e., electric conductivity and electronic structure). In addition, unsaturated selenium easily builds an acidic microenvironment on the catalyst surface, which is conducive to iron cycling and stable existence of sulfate radicals.

4. Conclusion

We have developed uniformed 2D superlattices comprising monolayer $FeSe_{2+x}$ @C nanocubes with unsaturated selenium via a spatially constrained topochemical transformation process by the Kirkendall effect and demonstrated their excellent application in Fenton-like reaction for environmental catalysis. We also have revealed the coordinative roles of cation and anion of the catalysts in catalysis. The 2D uniformed superlattice structure is able to expose more active sites while facilitating the large-scale transport and utilization of NC components. The 2D $FeSe_{2+x}$ @C NCSLs synergistically combine the advantages of superlattice materials and unsaturated selenium. Experiment and theoretical calculations show that unsaturated selenium can optimize the electronic structure of Fe active centers, not only promoting the Fe^{3+}/Fe^{2+} cycle, regulating PMS adsorption, and lowering reaction energy barrier, but also generating an acidic microenvironment on the catalyst surface for enhancing its catalytic activity. The catalyst can rapidly activate PMS to yield $SO_4^{\bullet-}$ to degrade various refractory pollutants (DIA, TC, IOH, TM, and SMZ) with excellent stability and adaptability. This spatially constrained topochemical transformation approach is facile and scalable, and this work supplies valuable guidance for the development of various functionalized 2D porous NC superlattices as catalysts for their industrial applications in the future.

CRediT authorship contribution statement

Qiang Zhong: Conceptualization, Methodology, Investigation, Writing – original draft, Validation, Formal analysis, Visualization, Software. **Yue Sun:** Data curation, Investigation, Software. **Shixi Wu:** Data curation. **Chenmin Xu:** Writing – review & editing, Funding acquisition. **Shaogui Yang:** Resources, Writing – review & editing, Funding acquisition. **Yazi Liu:** Data curation. **Dunyu Sun:** Data curation. **Bing Yang:** Data curation. **Chengdu Qi:** Data curation. **Zhe Xu:** Data curation. **Huan He:** Resources, Writing – review & editing, Funding acquisition. **Shiyin Li:** Data curation. **Shaobin Wang:** Writing – review & editing, Formal analysis, Validation.

Declaration of Competing Interest

The authors declare that they have no known competing financial interests or personal relationships that could have appeared to influence the work reported in this paper.

Data Availability

Data will be made available on request.

Appendix A. Supporting information

Supplementary data associated with this article can be found in the online version at doi:10.1016/j.apcatb.2022.122357.

References

[1] M.J. Klemes, Y. Ling, C. Ching, C. Wu, L. Xiao, D.E. Helbling, W.R. Dichtel, Reduction of a tetrafluoroterephthalonitrile-beta-cyclodextrin polymer to remove anionic micropollutants and perfluorinated alkyl substances from water, Angew. Chem. Int. Ed. 58 (2019) 12049–12053, https://doi.org/10.1002/anie.201905142.

[2] L. Gan, Q. Zhong, A. Geng, L. Wang, C. Song, S. Han, J. Cui, L. Xu, Cellulose derived carbon nanofiber: a promising biochar support to enhance the catalytic performance of $CoFe_2O_4$ in activating peroxymonosulfate for recycled dimethyl phthalate degradation, Sci. Total Environ. 694 (2019), 133705, https://doi.org/10.1016/j.scitotenv.2019.133705.

[3] H. Zhou, H. Zhang, Y. He, B. Huang, C. Zhou, G. Yao, B. Lai, Critical review of reductant-enhanced peroxide activation processes: Trade-off between accelerated Fe^{3+}/Fe^{2+} cycle and quenching reactions, Appl. Catal. B-Environ. 286 (2021), 119900, https://doi.org/10.1016/j.apcatb.2021.119900.

[4] X. Long, Z. Xiong, R. Huang, Y. Yu, P. Zhou, H. Zhang, G. Yao, B. Lai, Sustainable Fe(III)/Fe(II) cycles triggered by co-catalyst of weak electrical current in Fe(III)/peroxymonosulfate system: collaboration of radical and non-radical mechanisms, Appl. Catal. B-Environ. 317 (2022), 121716, https://doi.org/10.1016/j.apcatb.2022.121716.

[5] L.S. Zhang, X.H. Jiang, Z.A. Zhong, L. Tian, Q. Sun, Y.T. Cui, X. Lu, J.P. Zou, S. L. Luo, Carbon nitride supported high-loading fe single-atom catalyst for activating of peroxymonosulfate to generate $O_2^{\frac{1}{2}}$ with 100% selectivity, Angew. Chem. Int. Ed. 60 (2021) 21751–21755, https://doi.org/10.1002/anie.202109488.

[6] S. Zuo, X. Jin, X. Wang, Y. Lu, Q. Zhu, J. Wang, W. Liu, Y. Du, J. Wang, Sandwich structure stabilized atomic Fe catalyst for highly efficient Fenton-like reaction at all pH values, Appl. Catal. B-Environ. 282 (2021) 119551, https://doi.org/10.1016/j.apcatb.2020.119551.

[7] S. Liu, D. Liu, Y. Sun, P. Xiao, H. Lin, J. Chen, X.L. Wu, X. Duan, S. Wang, Enzyme-mimicking single-atom FeN4 sites for enhanced photo-Fenton-like reactions, Appl. Catal. B-Environ. 310 (2022), 121327, https://doi.org/10.1016/j.apcatb.2022.121327.

[8] K. Zhang, Z. Hu, X. Liu, Z. Tao, J. Chen, FeSe$_2$ microspheres as a high-performance anode material for Na-Ion batteries, Adv. Mater. 27 (2015) 3305–3309, https://doi.org/10.1002/adma.201500196.

[9] P. Ge, H. Hou, S. Li, L. Yang, X. Ji, Tailoring rod-like FeSe$_2$ coated with nitrogen-doped carbon for high-performance sodium storage, Adv. Funct. Mater. 28 (2018), 1801765, https://doi.org/10.1002/adfm.201801765.

[10] Q. Zhong, C. Xu, Y. Liu, Q. Ji, Z. Xu, D. Sun, S. Zhou, B. Yang, Y. Dai, C. Qi, S. Yang, H. He, S. Li, C. Sun, Defect-engineered FeSe$_{2-x}$@C with porous architecture for enhanced peroxymonosulfate-based advanced oxidation processes, Appl. Catal. B-Environ. 309 (2022), 121259, https://doi.org/10.1016/j.apcatb.2022.121259.

[11] G. Fang, T. Zhang, H. Cui, D.D. Dionysiou, C. Liu, J. Gao, Y. Wang, D. Zhou, Synergy between iron and selenide on FeSe$_2$(111) surface driving peroxymonosulfate activation for efficient degradation of pollutants, Environ. Sci. Technol. 54 (2020) 15489–15498, https://doi.org/10.1021/acs.est.0c06091.

[12] Y. Deng, X. Xi, Y. Xia, Y. Cao, S. Xue, S. Wan, A. Dong, D. Yang, 2D FeP nanoframe superlattices via space-confined topochemical transformation, Adv. Mater. 34 (2022), 2109145, https://doi.org/10.1002/adma.202109145.

[13] L. Yu, X.Y. Yu, X.W. Lou, The design and synthesis of hollow micro-/nanostructures: present and future trends, Adv. Mater. 30 (2018), 1800939, https://doi.org/10.1002/adma.201800939.

[14] G. Zhan, P. Li, H.C. Zeng, Architectural designs and synthetic strategies of advanced nanocatalysts, Adv. Mater. 30 (2018), 1802094, https://doi.org/10.1002/adma.201802094.

[15] Z. Wang, E. Almatrafi, H. Wang, H. Qin, W. Wang, L. Du, S. Chen, G. Zeng, P. Xu, Cobalt single atoms anchored on oxygen-doped tubular carbon nitride for efficient peroxymonosulfate activation: simultaneous coordination structure and morphology modulation, Angew. Chem. Int. Ed. 61 (2022) 1433–7851, https://doi.org/10.1002/anie.202202338.

[16] Y. Jiao, D. Han, Y. Ding, X. Zhang, G. Guo, J. Hu, D. Yang, A. Dong, Fabrication of three-dimensionally interconnected nanoparticle superlattices and their lithium-ion storage properties, Nat. Commun. 6 (2015) 6420, https://doi.org/10.1038/ncomms7420.

[17] P. Li, Y. Lin, S. Zhao, Y. Fu, W. Li, R. Chen, S. Tian, Defect-engineered Co$_3$O$_4$ with porous multishelled hollow architecture enables boosted advanced oxidation processes, Appl. Catal. B-Environ. 298 (2021), 120596, https://doi.org/10.1016/j.apcatb.2021.120596.

[18] P.J. Santos, R.J. Macfarlane, Reinforcing supramolecular bonding with magnetic dipole interactions to assemble dynamic nanoparticle superlattices, J. Am. Chem. Soc. 142 (2020) 1170–1174, https://doi.org/10.1021/jacs.9b11476.

[19] Y. Deng, Y. Cao, Y. Xia, X. Xi, Y. Wang, W. Jiang, D. Yang, A. Dong, T. Li, Self-templated synthesis of CoFeP @ C cage-in-cage superlattices for enhanced electrocatalytic water splitting, Adv. Mater. (2022), 2202394, https://doi.org/10.1002/aenm.202202394.

[20] J. Chen, A. Dong, J. Cai, X. Ye, Y. Kang, J.M. Kikkawa, C.B. Murray, Collective dipolar interactions in self-assembled magnetic binary nanocrystal superlattice membranes, Nano Lett. 10 (2010) 5103–5108, https://doi.org/10.1021/nl103568q.

[21] F. Fetzer, A. Maier, M. Hodas, O. Geladari, K. Braun, A.J. Meixner, F. Schreiber, A. Schnepf, M. Scheele, Structural order enhances charge carrier transport in self-assembled Au-nanoclusters, Nat. Commun. 11 (2020) 6188, https://doi.org/10.1038/s41467-020-19461-x.

[22] B. Jang, M. Park, O.B. Chae, S. Park, Y. Kim, S.M. Oh, Y. Piao, T. Hyeon, Direct synthesis of self-assembled ferrite/carbon hybrid nanosheets for high performance lithium-ion battery anodes, J. Am. Chem. Soc. 134 (2012) 15010–15015, https://doi.org/10.1021/ja305539r.

[23] M. Kobayashi, J. Ueno, M. Enami, S. Katsuta, A. Ichiba, K. Ogura, K. Onomitsu, Y. Horikoshi, Growth and UV-A sensor applications of MgCdS/ZnCdS superlattices, J. Cryst. Growth 278 (2005) 273–277, https://doi.org/10.1016/j.jcrysgro.2005.01.032.

[24] M.A. Boles, M. Engel, D.V. Talapin, Self-assembly of colloidal nanocrystals: from intricate structures to functional materials, Chem. Rev. 116 (2016) 11220–11289, https://doi.org/10.1021/acs.chemrev.6b00196.

[25] J. Shim, F.S. Bates, T.P. Lodge, Superlattice by charged block copolymer selfassembly, Nat. Commun. 10 (2019) 2108, https://doi.org/10.1038/s41467-019-10141-z.

[26] T. Li, B. Xue, B. Wang, G. Guo, D. Han, Y. Yan, A. Dong, Tubular monolayer superlattices of hollow Mn$_3$O$_4$ nanocrystals and their oxygen reduction activity, J. Am. Chem. Soc. 139 (2017) 12133–12136, https://doi.org/10.1021/jacs.7b06587.

[27] J. Zhang, X. Mao, S. Wang, L. Liang, M. Cao, L. Wang, G. Li, Y. Xu, X. Huang, Superlattice in a Ru superstructure for enhancing hydrogen evolution, Angew. Chem. Int. Ed. 134 (2022), 2116867, https://doi.org/10.1002/anie.202116867.

[28] H. Li, H. Zu, Q. Li, J. Yang, W. Qu, Z. Yang, Coordinatively unsaturated selenides over CuFeSe$_2$ toward highly efficient mercury immobilization, Environ. Sci. Technol. 56 (2022) 575–584, https://doi.org/10.1021/acs.est.1c05337.

[29] D. Gao, J. Xu, F. Chen, P. Wang, H. Yu, Unsaturated selenium-enriched MoSe$_{2+x}$ amorphous nanoclusters: one-step photoinduced co-reduction route and its boosted photocatalytic H$_2$ evolution activity for TiO$_2$, Appl. Catal. B-Environ. 305 (2022), 121053, https://doi.org/10.1016/j.apcatb.2021.121053.

[30] L. Zhang, C. Lu, F. Ye, R. Pang, Y. Liu, Z. Wu, Z. Shao, Z. Sun, L. Hu, Selenic acid etching assisted vacancy engineering for designing highly active electrocatalysts toward the oxygen evolution reaction, Adv. Mater. 33 (2021) 2007523, https://doi.org/10.1002/adma.202007523.

[31] C. An, Y. Yuan, B. Zhang, L. Tang, B. Xiao, Z. He, J. Zheng, J. Lu, Graphene wrapped FeSe$_2$ nano-microspheres with high pseudocapacitive contribution for

[32] Q. Yan, C. Lian, K. Huang, L. Liang, H. Yu, P. Yin, J. Zhang, M. Xing, Constructing an acidic microenvironment by MoS$_2$ in heterogeneous fenton reaction for pollutant control, Angew. Chem. Int. Ed. 60 (2021) 17155–17163, https://doi.org/10.1002/anie.202105736.

[33] W. Zhong, X. Wu, Y. Liu, X. Wang, J. Fan, H. Yu, Simultaneous realization of sulfur-rich surface and amorphous nanocluster of NiS$_{1+x}$ cocatalyst for efficient photocatalytic H$_2$ evolution, Appl. Catal. B-Environ. 280 (2021), 119455, https://doi.org/10.1016/j.apcatb.2020.119455.

[34] X. Zhang, F. Zhou, S. Zhang, Y. Liang, R. Wang, Engineering MoS$_2$ basal planes for hydrogen evolution via synergistic ruthenium doping and nanocarbon hybridization, Adv. Sci. 6 (2019), 1900090, https://doi.org/10.1002/advs.201900090.

[35] K. Chang, Z. Mei, T. Wang, Q. Kang, S. Ouyang, J. Ye, MoS$_2$/graphene cocatalyst for efficient photocatalytic H2 evolution under visible light irradiation, ACS Nano 8 (2014) 7078–7087, https://doi.org/10.1021/nn5019945.

[36] G. Kresse, D. Joubert, From ultrasoft pseudopotentials to the projector augmented-wave method, Phys. Rev. B 59 (1999) 1758–1775, https://doi.org/10.1103/PhysRevB.59.1758.

[37] G. Kresse, J. Furthmüller, Efficiency of ab-initio total energy calculations for metals and semiconductors using a plane-wave basis set, Comp. Mater. Sci. 6 (1996) 15–50, https://doi.org/10.1016/0927-0256(96)00008-0.

[38] Furthmuller Kresse, Efficient iterative schemes for ab initio total-energy calculations using a plane-wave basis set, Phys. Rev. 54 (1996) 11169, https://doi.org/10.1103/PhysRevB.54.11169.

[39] S. Grimme, J. Antony, S. Ehrlich, H. Krieg, A consistent and accurate ab initio parametrization of density functional dispersion correction (DFT-D) for the 94 elements H-Pu, J. Chem. Phys. 132 (2010), 154104, https://doi.org/10.1063/1.3382344.

[40] L. Li, L. Zhu, L.H. Xu, T.M. Cheng, W. Wang, X. Li, Q.-T. Sui, Site-exchange of Li and M ions in silicate cathode materials Li$_2$MSiO$_4$ (M = Mn, Fe, Co and Ni): DFT calculations, J. Mater. Chem. A 2 (2014) 4251–4255, https://doi.org/10.1039/c3ta14885h.

[41] W. Xu, W. Xue, H. Huang, J. Wang, C. Zhong, D. Mei, Morphology controlled synthesis of alpha-Fe$_2$O$_{3-x}$ with benzimidazole-modified Fe-MOFs for enhanced photo-Fenton-like catalysis, Appl. Catal. B-Environ. 291 (2021), 120129, https://doi.org/10.1016/j.apcatb.2021.120129.

[42] M. Zhang, C. Xiao, X. Yan, S. Chen, C. Wang, R. Luo, J. Qi, X. Sun, L. Wang, J. Li, Efficient removal of organic pollutants by metal-organic framework derived Co/C yolk-shell nanoreactors: size-exclusion and confinement effect, Environ. Sci. Technol. 54 (2020) 10289–10300, https://doi.org/10.1021/acs.est.0c00914.

[43] L. Qin, H. Ye, C. Lai, S. Liu, X. Zhou, F. Qin, D. Ma, B. Long, Y. Sun, L. Tang, M. Yan, W. Chen, W. Chen, L. Xiang, Citrate-regulated synthesis of hydrotalcite-like compounds as peroxymonosulfate activator - Investigation of oxygen vacancies and degradation pathways by combining DFT, Appl. Catal. B-Environ. 317 (2022), 121704, https://doi.org/10.1016/j.apcatb.2022.121704.

[44] C. He, S. Wu, N. Zhao, C. Shi, E. Liu, J. Li, Carbon-Encapsulated Fe$_3$O$_4$ Nanoparticles as a High-Rate Lithium Ion Battery Anode Material, Acs Nano 7 (2013) 4459–4469, https://doi.org/10.1021/nn401059h.

[45] P. Li, Y. Lin, Q. Huang, W. Li, S. Zhao, Y. Fu, F. Chu, S. Tian, Coordination environment and architecture engineering over Co4N-based nanocomposite for accelerating advanced oxidation processes, Appl. Catal. B-Environ. 302 (2022), 120850, https://doi.org/10.1016/j.apcatb.2021.120850.

[46] X. Mao, J.G. Kim, J. Han, H.S. Jung, S.G. Lee, N.A. Kotov, J. Lee, Phase-Pure FeSe$_x$ (x=1, 2) nanoparticles with one- and two-photon luminescence, J. Am. Chem. Soc. 136 (2014) 7189–7192, https://doi.org/10.1021/ja412654c.

[47] Y. Wang, Y. Zhang, R. Shao, Q. Guo, FeSe and Fe$_3$Se$_4$ encapsulated in mesoporous carbon for flexible solid-state supercapacitor, Chem. Eng. J. 442 (2022), 136362, https://doi.org/10.1016/j.cej.2022.136362.

[48] W. Zhao, X. Ma, L. Yue, L. Zhang, Y. Luo, Y. Ren, X.-E. Zhao, N. Li, B. Tang, Q. Liu, Y. Liu, S. Gao, A.A. Alshehri, X. Sun, A gradient hexagonal-prism Fe$_3$Se$_4$@SiO$_2$@C configuration as a highly reversible sodium conversion anode, J. Mater. Chem. A 10 (2022) 4087–4099, https://doi.org/10.1039/d1ta10571j.

[49] J. Yuan, Y. Gan, X. Xu, M. Mu, H. He, X. Li, X. Zhang, J. Liu, Construction of Fe$_7$Se$_8$@Carbon nanotubes with enhanced sodium/potassium storage, J. Colloid Interf. Sci. 626 (2022) 355–363, https://doi.org/10.1016/j.jcis.2022.06.139.

[50] Y. Liu, C. Yang, Y. Li, F. Zheng, Y. Li, Q. Deng, W. Zhong, G. Wang, T. Liu, FeSe$_2$/nitrogen-doped carbon as anode material for Potassium-ion batteries, Chem. Eng. J. 393 (2020), 124590, https://doi.org/10.1016/j.cej.2020.124590.

[51] J. Liang, L. Fu, K. Gao, X. Duan, Accelerating radical generation from peroxymonosulfate by confined variable Co species toward ciprofloxacin mineralization: ROS quantification and mechanisms elucidation, Appl. Catal. B Environ. 315 (2022), 121542, https://doi.org/10.1016/j.apcatb.2022.121542.

[52] Y. Lei, X. Guo, M. Jiang, W. Sun, H. He, Y. Chen, K. Thummavichai, O. Ola, Y. Zhu, N. Wang, Co-ZIF reinforced cow manure biochar (CMB) as an effective peroxymonosulfate activator for degradation of carbamazepine, Appl. Catal. B Environ. 319 (2022), 121932, https://doi.org/10.1016/j.apcatb.2022.121932.

[53] M.N. Sugihara, D. Moeller, T. Paul, T.J. Strathmann, TiO$_2$-photocatalyzed transformation of the recalcitrant X-ray contrast agent diatrizoate, Appl. Catal. B-Environ. 129 (2013) 114–122, https://doi.org/10.1016/j.apcatb.2012.09.013.

[54] C. Zhu, Y. Nie, F. Cun, Y. Wang, Z. Tian, F. Liu, Two-step pyrolysis to anchor ultrahigh-density single-atom FeN$_5$ sites on carbon nitride for efficient Fenton-like catalysis near 0 °C, Appl. Catal. B-Environ. 319 (2022), 121900, https://doi.org/10.1016/j.apcatb.2022.121900.

[55] W. Xiang, Q. Ji, C. Xu, Y. Guo, Y. Liu, D. Sun, W. Zhou, Z. Xu, C. Qi, S. Yang, S. Li, C. Sun, H. He, Accelerated photocatalytic degradation of iohexol over Co_3O_4/g-C_3N_4/$Bi_2O_2CO_3$ of p-n/n-n dual heterojunction under simulated sunlight by persulfate, Appl. Catal. B-Environ. 285 (2021), 119847, https://doi.org/10.1016/j.apcatb.2020.119847.

[56] Z.-Y. Guo, C.-X. Li, M. Gao, X. Han, Y.-J. Zhang, W.-J. Zhang, W.-W. Li, Mn-O covalency governs the intrinsic activity of co-mn spinel oxides for boosted peroxymonosulfate activation, Angew. Chem. Int. Ed. 60 (2021) 274–280, https://doi.org/10.1002/anie.202010828.

[57] P. Duan, X. Xu, K. Guo, Q. Yue, B. Gao, Peroxymonosulfate activation on a chainmail catalyst via an electron shuttle mechanism for efficient organic pollutant removal, Appl. Catal. B-Environ. 316 (2022) 121695, https://doi.org/10.1016/j.apcatb.2022.121695.

[58] M. Xie, F. Dai, J. Li, X. Dang, J. Guo, W. Lv, Z. Zhang, X. Lu, Tailoring the electronic metal-support interactions in supported atomically dispersed gold catalysts for efficient fenton-like reaction, Angew. Chem. Int. Ed. 60 (2021) 14370–14375, https://doi.org/10.1002/anie.202103652.

[59] Y. Chen, G. Zhang, H. Liu, J. Qu, Confining free radicals in close vicinity to contaminants enables ultrafast fenton-like processes in the interspacing of MoS_2 membranes, Angew. Chem. Int. Ed. 58 (2019) 8134–8138, https://doi.org/10.1002/anie.201903531.

[60] R. Zhu, Y. Zhu, H. Xian, L. Yan, H. Fu, G. Zhu, Y. Xi, J. Zhu, H. He, CNTs/ferrihydrite as a highly efficient heterogeneous Fenton catalyst for the degradation of bisphenol A: the important role of CNTs in accelerating Fe (III)/Fe(II) cycling, Appl. Catal. B-Environ. 270 (2020), 118891, https://doi.org/10.1016/j.apcatb.2020.118891.

[61] T. Li, Y. Chen, X. Wang, J. Liang, L. Zhou, Modifying organic carbon in Fe_3O_4-loaded schwertmannite to improve heterogeneous Fenton activity through accelerating Fe(II) generation, Appl. Catal. B Environ. 285 (2021), 119830, https://doi.org/10.1016/j.apcatb.2020.119830.

[62] Z. Wu, Y. Wang, Z. Xiong, Z. Ao, S. Pu, G. Yao, B. Lai, Core-shell magnetic Fe_3O_4@Zn/Co-ZIFs to activate peroxymonosulfate for highly efficient degradation of carbamazepine, Appl. Catal. B Environ. 277 (2020), 119136, https://doi.org/10.1016/j.apcatb.2020.119136.

[63] I.S. Kwon, I.H. Kwak, T.T. Debela, H.G. Abbas, Y.C. Park, J.-P. Ahn, J. Park, H.S. Kang, Se-Rich $MoSe_2$ nanosheets and their superior electrocatalytic performance for hydrogen evolution reaction, ACS Nano 14 (2020) 6295–6304, https://doi.org/10.1021/acsnano.0c02593.

[64] L. Wu, Z. Sun, Y. Zhen, S. Zhu, C. Yang, J. Lu, Y. Tian, D. Zhong, J. Ma, Oxygen vacancy-induced nonradical degradation of organics: critical trigger of oxygen (O_2) in the Fe-Co LDH/peroxymonosulfate system, Environ. Sci. Technol. 55 (2021) 15400–15411, https://doi.org/10.1021/acs.est.1c04600.

[65] K. Guo, Y. Zhu, Z. Yan, A. Liu, X. Du, X. Wang, W. Tan, L. Li, J. Sun, Q. Tong, C. Tang, L. Dong, The dual effects of ammonium bisulfate on the selective catalytic reduction of NO with NH_3 over Fe_2O_3-WO_3 catalyst confined in MCM-41, Chem. Eng. J. 389 (2020), 124271, https://doi.org/10.1016/j.cej.2020.124271.